

1 **Estimating CCN number concentrations using aerosol optical properties:**

2 **Role of particle number size distribution and parameterization**

3
4 Yicheng Shen^{1,2}, Aki Virkkula^{2,1,3}, Aijun Ding¹, Krista Luoma², Helmi Keskinen^{2,4},
5 Pasi P. Aalto², Xuguang Chi¹, Ximeng Qi¹, Wei Nie¹, Xin Huang¹,
6 Tuukka Petäjä^{2,1}, Markku Kulmala², Veli-Matti Kerminen²

7
8 ¹Joint International Research Laboratory of Atmospheric Sciences, School of Atmospheric Sciences,
9 Nanjing University, Nanjing, 210023, China

10 ²Institute for Atmospheric and Earth System Research, University of Helsinki, Helsinki, Finland

11 ³Finnish Meteorological Institute, Helsinki, Finland

12 ⁴Hyytiälä Forestry Field Station, Hyytiäläntie 124, Korkeakoski FI 35500, Finland

13
14 Keywords: CCN, scattering coefficient, backscatter fraction, Ångström exponent

15
16 **Abstract**

17 The concentration of cloud condensation nuclei (CCN) is an essential parameter affecting
18 aerosol-cloud interactions within warm clouds. Long-term CCN number concentration (N_{CCN})
19 data are scarce, there are a lot more data on aerosol optical properties (AOPs). It is therefore
20 valuable to derive parameterizations for estimating N_{CCN} from AOP measurements. Such
21 parameterizations have been made earlier, and in the present work a new one is presented. The
22 relationships between N_{CCN} , AOPs and size distributions were investigated based on in-situ
23 measurement data from six stations in very different environments around the world. The
24 relationships were used for deriving a parameterization that depends on the scattering Ångström
25 exponent (SAE), backscatter fraction (BSF) and total scattering coefficient (σ_{sp}) of PM10
26 particles. **The analysis first showed that the dependence of N_{CCN} on supersaturation SS is**
27 **logarithmic in the range $SS < 1.1\%$.** The relationships between N_{CCN} and AOPs were
28 parameterized as: $N_{CCN} \approx ((286 \pm 46)SAE \ln(SS/(0.093 \pm 0.006))(BSF - BSF_{min}) + (5.2 \pm 3.3))\sigma_{sp}$,
29 where BSF_{min} is the minimum BSF, in practice the 1st percentile of BSF data at a site to be
30 analyzed. At the lowest supersaturations of each site ($SS \approx 0.1\%$), the average bias, defined as

1 the ratio of the AOP-derived and measured N_{CCN} varied from ~ 0.7 to ~ 1.5 at most sites except
2 at a Himalayan site where bias was > 4 . At $SS > 0.3\%$ the average bias ranged from ~ 0.7 to
3 ~ 1.3 at all sites. In other words, at $SS > 0.3\%$ N_{CCN} was estimated with an average uncertainty
4 of approximately 30% by using nephelometer data. The squared correlation coefficients
5 between the AOP-derived and measured N_{CCN} varied from ~ 0.5 to ~ 0.8 . To study the physical
6 explanation of the relationships between N_{CCN} and AOPs, lognormal unimodal particle size
7 distributions were generated and N_{CCN} and AOPs were calculated. The simulation showed that
8 the relationships of N_{CCN} and AOPs are affected by the geometric mean diameter and width of
9 the size distribution and the activation diameter. The relationships of N_{CCN} and AOPs were
10 similar to those of the observed ones.

11

12 **1. Introduction**

13 Aerosol-cloud interactions (ACI) are the most significant sources of uncertainty in estimating
14 the radiative forcing of the Earth's climate system (e.g., Forster et al., 2007; Kerminen et al.,
15 2012), which makes it more challenging to predict the future climate change (Schwartz et al.,
16 2010). An essential parameter affecting ACI within warm clouds is the concentration of cloud
17 condensation nuclei (CCN), i.e., the number concentration of particles capable of initiating
18 cloud droplet formation at a given supersaturation. Determining CCN concentrations and their
19 temporal and spatial variations is one of the critical aspects to reduce such uncertainty.

20

21 CCN number concentrations (N_{CCN}) have been measured at different locations worldwide (e.g.,
22 Twomey, 1959; Hudson, 1993; Kulmala et al., 1993; Hämeri et al., 2001; Sihto et al., 2011;
23 Pöhlker et al., 2016; Ma et al., 2014). However, the accessible data especially for long-term
24 measurements are still limited in the past and nowadays due to the relatively high cost of
25 instrumentation and the complexity of long-term operating. As an alternative to direct
26 measurement, N_{CCN} can also be estimated from particle number size distributions and chemical
27 composition using the Köhler equation. Several studies have investigated the relative
28 importance of the chemical composition and particle number distributions for the estimation of
29 N_{CCN} (Dusek et al., 2006; Ervens et al., 2007; Hudson, 2007; Crosbie et al., 2015). For the best
30 of our understanding, particle number size distributions are more important in determining N_{CCN}

1 than aerosol chemical composition. This makes particle number size distribution measurements
2 capable of serving as a supplement to direct CCN measurements.

3
4 Considering the tremendous spatiotemporal heterogeneity of atmospheric aerosol, neither
5 direct measurements of N_{CCN} nor the concentrations estimated from particle size distributions
6 are adequate for climate research. In order to overcome the limitation of current measurements,
7 many studies have attempted to estimate N_{CCN} using aerosol optical properties (AOPs) (e.g.,
8 Ghan et al., 2006; Shinozuka et al., 2009; Andreae, 2009; Jefferson, 2010; Liu et al., 2014;
9 Shinozuka et al., 2015; Tao et al., 2018). This approach would give both geographically wider
10 and temporally longer estimates of N_{CCN} than the available particle number size distribution and
11 direct CCN measurement data. For instance, on 20 June 2019 the WMO Global Atmosphere
12 Watch World Data Centre for Aerosols (GAW-WDCA) (<http://ebas.nilu.no/>) contained particle
13 number size distribution data sets from 22 countries altogether from 58 stations, but only 5 of
14 them were outside Europe. The CCN counter (CCNC) data were from 3 European sites. On the
15 other hand, in the same data base, the light scattering coefficients measured with a nephelometer
16 were from 31 countries and 103 stations located on all continents and also on some islands. The
17 temporal coverage data in the GAW-WDCA data base is such that the oldest nephelometer data,
18 those from Mauna Loa, start in 1974, whereas the oldest particle number size distribution data,
19 those from the SMEAR II station in Finland, start in 1993. Another easily available source for
20 data is the US Department of Energy Atmospheric Radiation Measurement (ARM) user facility
21 (<https://www.arm.gov/data>). On 20 June 2019 we found that the ARM research facility data
22 contained particle size distribution data from 7 permanent sites and light scattering coefficient
23 measured with a nephelometer from 20 sites. It is clear that there are other data sets of all of
24 these measured around the world, but those that can be found either from the GAW-WDCA or
25 the ARM data bases are quality controlled and readily available.

26
27 Most of the above-mentioned studies attempted to link N_{CCN} with extensive AOPs, such as the
28 aerosol extinction coefficient (σ_{ext}), aerosol scattering coefficient (σ_{sp}) and aerosol optical depth
29 (AOD). Both N_{CCN} and σ_{sp} are extensive properties that vary with a varying aerosol loading.
30 The most straightforward approach to estimate CCN is to utilize the ratio between CCN and

1 one of the extensive AOPs (e.g. AOD, σ_{ext} , σ_{sp}). However, the ratio is not a constant. Previous
2 studies have also pointed out that the relationship between N_{CCN} and extensive AOPs are
3 nonlinear. On one hand, Andreae (2009) reported that the relationship between AOD and CCN
4 number concentration at the supersaturation of 0.4% ($\text{CCN}_{0.4}$) can be written as
5 $\text{AOD}_{500}=0.0027 \cdot (\text{CCN}_{0.4})^{0.640}$, which indicates that AOT and CCN depend in a non-linear way
6 on each other: for a larger AOD there are more CCN per-unit change in AOD. On the other
7 hand, Shinozuka et al. (2015) indicated that the larger the extinction coefficient σ_{ext} was, the
8 fewer CCN were per unit change of σ_{ext} .

9

10 Some studies have also involved intensive aerosol optical properties, such as the scattering
11 Ångström exponent (SAE), hemispheric backscattering fraction (BSF) and single-scattering
12 albedo (SSA) to build up a bridge between the N_{CCN} and AOPs. Jefferson (2010) used BSF and
13 SSA to parameterize the coefficients C and k in the relation $N_{\text{CCN}}(\text{SS}) = C \times (\text{SS})^k$, where SS is
14 the supersaturation percent (Twomey, 1959) and the exponent k is a function of SSA which
15 means it depends both on the scattering and absorption coefficients. Liu and Li (2014) discussed
16 how different aerosol properties affect the ratio of N_{CCN} to σ_{sp} , i.e., $R_{\text{CCN}}/\sigma_{\text{sp}}$ based on *in-situ*
17 and remote-sensing data. Shinozuka et al. (2015) used SAE and aerosol extinction coefficient
18 to estimate N_{CCN} . Tao et al. (2018) used a novel method to derive the ratio $R_{\text{CCN}}/\sigma_{\text{sp}}$ which they
19 named as AR_{sp} , based on SAE and aerosol hygroscopicity using a humidified nephelometer.
20 All the studies mentioned above noted that the particle number size distribution (PNSD) plays
21 an important role in estimating N_{CCN} from aerosol optical properties.

22

23 In this paper we will analyze the relationships between N_{CCN} , aerosol optical properties and size
24 distributions at six different types of sites around the world. The relationships obtained from
25 the field sites will be used for developing a parameterization for calculating N_{CCN} using AOPs.
26 We will also study the physical explanations of the relationships between N_{CCN} and AOPs by
27 simulations.

28

29

30

2. Methods

2.1 Sites and measurements

In-situ measurements of AOPs, particle number size distributions (PNSDs), and N_{CCN} were conducted at SMEAR II in Finland, SORPES in China, and 4 ARM Climate Research Facility (ACRF) sites (Mather and Voyles, 2013). The locations and measurement periods are listed in Table 1.

The Station for Measuring Forest Ecosystem-Atmosphere Relations (**SMEAR II**) is located at the Hyytiälä Forestry Field Station (61°51' N, 24°17' E, 181 m above sea level) of University of Helsinki, 60 km north-east from the nearest city. The station represents boreal coniferous forest, which covers ~8 % of the Earth's surface. Total scattering coefficient (σ_{sp}) and hemispheric backscattering coefficient (σ_{bsp}) of sub-1 μm and sub-10 μm particles are measured using a TSI-3563 3-wavelength integrating nephelometer at $\lambda = 450, 550, \text{ and } 700 \text{ nm}$. The calibration, data processing and calculation of AOPs followed the procedure described by Virkkula et al. (2011) and Luoma et al. (2019). N_{CCN} was measured at the supersaturations (SS) of 0.1%, 0.2%, 0.3%, 0.5% and 1.0% using a DMT CCN-100 CCN counter, similar to Schmale et al. (2017). A whole measurement cycle takes around 2 hours; data were interpolated to hourly time resolution to compare with other measurements. PNSDs were measured with a custom-made Differential Mobility Particle Sizer (DMPS) system in size range 3–1000 nm (Aalto et al., 2001). A more detailed description of CCN measurements and station operation can be found in Sihto et al. (2011) and Paramonov et al. (2015).

The Station for Observing Regional Processes of the Earth System (**SORPES**) is located in a suburb of Nanjing, a megacity in the Yangtze River Delta municipal aggregation (32°07'14" N, 118°57'10" E; ~40m a.s.l.). σ_{sp} and σ_{bsp} of total suspended particles (TSP) were measured with an Ecotech Aurora-3000 3-wavelength integrating nephelometer at $\lambda = 450, 525, \text{ and } 635 \text{ nm}$ as described by Shen et al. (2018). N_{CCN} was measured using a CCN-200 dual column CCN counter at 5 supersaturations: 0.1%, 0.2%, 0.4%, 0.6% and 0.8%. The two columns make the same cycle simultaneously to cross-check with each other. Each cycle took 30 minutes. PNSDs in the size range of 6 - 800 nm were measured with a DMPS built by University of Helsinki.

1 More details of the measurements at SORPES are given by, e.g., Ding et al. (2013, 2016) and
2 Qi et al. (2015).

3

4 The US Atmospheric Radiation Measurement Mobile Facility (AMF) measures atmospheric
5 aerosol and radiation properties all over the world. The first AMF (AMF1) was deployed in
6 2005 with both a CCN counter and a nephelometer. Between 2011 and 2018, AMF1 was
7 operated at four locations: Ganges Valley (**PGH**) in the Himalayas, Cape Cod, Massachusetts
8 (**PVC**) in a coastal area of U.S., Manacapuru (**MAO**) downwind of the city of Manaus, Brazil,
9 and Ascension Island (**ASI**) on the South Atlantic Ocean downwind from Africa. Three of them
10 were accompanied by a scanning mobility particle sizer (SMPS; Kuang, 2016). The SMPS is
11 also part of the Aerosol Observing System (AOS) running side by side with AMF1 since 2012.
12 Both PNSDs and AOPs are available simultaneously at PVC, MAO, and ASI. σ_{sp} and σ_{bsp} of
13 sub-1 μm and sub-10 μm particles are measured at all AMF1 locations by integrating
14 nephelometers (Uin, 2016a). The size range of the SMPS is around 11 – 465 nm with slightly
15 different ranges for different periods. N_{CCN} is measured at different supersaturations, with the
16 details given in Table 1. The supersaturations are typically calibrated before and after each
17 campaign at an altitude similar to measurement site according to the CCN handbook (Uin,
18 2016b). Detailed information about each dataset and measurement site can be found in the AOS
19 handbook (Jefferson, 2011) or ARM web site (<http://www.arm.gov/>) and references thereby.

20

21 Ganges Valley (PGH) is located in one of the largest and most rapidly developing sections of
22 the Indian subcontinent. The aerosols in this region have complex sources, including coal
23 combustion; biomass burning; automobile emissions; and dust. In monsoon seasons, dust
24 dominates the aerosol mass due to transportation (Dumka et al., 2017; Gogoi et al., 2015).

25

26 PVC refers to the on-shore data set for the ‘first column’ of the Two-Column Aerosol Project
27 (TCAP) on Cape Cod, Massachusetts, USA. This is a coastal site but also significantly affected
28 by anthropogenic emissions (Berg et al., 2016).

29

30 MAO refers to Manacapuru in Amazonas, Brazil. **It is a relatively clean site where Manaus**

1 pollution plumes and biomass burning plumes impact the background pristine rainforest aerosol
2 alternately (e.g., de Sá et al., 2019).

3
4 Ascension Island (ASI) is located in the southeast Atlantic where westward transport of
5 biomass-burning aerosols from southern Africa may increase aerosol concentrations to high
6 levels. Air mass at this site usually a mixture with aged biomass-burning plume and sea-salt
7 aerosol. The aerosol loading can be very low when there is no pollution plume. In this case,
8 there is a substantial uncertainty on the backscatter fraction.

9
10 The primary purpose of this study is to use as basic and readily accessible measurement data as
11 possible to estimate N_{CCN} . Aerosol optical properties are measured at different cutoff diameters,
12 usually 1 μm , 2.5 μm , 10 μm or TSP. At several stations there are two sets of AOPs using two
13 cutoff diameters. For this study we chose to use AOP data with the 10 μm cutoff (if data for
14 both 10 μm and 1 μm are available) that is more commonly used than smaller cutoff diameters.

15 16 **2.2 Data processing**

17 Regardless of the time resolution of raw data, all the data in this study were adjusted into hourly
18 averages before further analyses. Suspicious data within the whole dataset were removed
19 according to the following criteria:

- 20
- 21 1) for the size distributions, all the data with unexplainable spikes were removed manually;
 - 22 2) for CCN measurements, insufficient water supply may cause underestimation of CCN,
23 especially at lower supersaturations (DMT, 2009). N_{CCN} reading at lower SS has a sudden drop
24 a few hours before the similar sudden drop for higher SS under such conditions, so data from
25 such periods were removed;
 - 26 3) if any obvious inconsistencies between the AOPs and PNSD or between the N_{CCN} and PNSD
27 were found on closure study, all the data in the same hour were removed.

28
29 Special treatments were carried out for the ASI dataset. There will inevitably be a considerable
30 uncertainty in the backscattering fraction if the zero point of either σ_{sp} or σ_{bsp} is inaccurate in

1 very clean conditions. The measured σ_{sp} was in agreement with that calculated from the PNSD
2 with the Mie model. However, in the data σ_{bsp} approaches 0.3 Mm^{-1} whenever σ_{sp} approaches
3 0. Thus, we subtracted from back scattering coefficients a constant 0.3 Mm^{-1} and no longer used
4 any data points with $\sigma_{sp} < 2 \text{ Mm}^{-1}$ for this site to assure the data quality.

5
6 A more detailed description of the total number of available hourly-averaged data, accepted
7 data and removed data and the fractions of these are presented the supplement S1.

8 9 **2.3 Optical properties calculated from the nephelometer data**

10 **The hemispheric backscatter fraction BSF was calculated from**

$$11 \quad \text{BSF} = \frac{\sigma_{bsp}}{\sigma_{sp}} \quad (1)$$

12 where σ_{sp} and σ_{bsp} are the total scattering coefficient and backscattering coefficient, respectively.
13 BSF depends on both particle size and shape. For very small particles, BSF approaches the
14 value of 0.5 and decreases with an increasing particle size (e.g., Wiscombe and Grams, 1976;
15 Horvath et al., 2016; Shen et al., 2018). Jefferson (2010) used BSF as a proxy for the particle
16 size for estimating CCN concentrations from in situ AOP measurements.

17
18 **Scattering Ångström exponent (SAE) was calculated from total scattering coefficients σ_{sp} at**
19 **wavelengths λ_1 and λ_2 from**

$$20 \quad \text{SAE} = -\frac{\log(\sigma_{sp}(\lambda_1)) - \log(\sigma_{sp}(\lambda_2))}{\log(\lambda_1) - \log(\lambda_2)} \quad (2)$$

21 **For those sites where the TSI 3563 nephelometer was used the wavelength pair was 450 nm**
22 **and 700 nm, for the Ecotech Aurora-3000 nephelometer the wavelength pair was 450 nm and**
23 **635 nm. SAE is typically considered to be associated with the dominating particle size. Its large**
24 **values (e.g. $\text{SAE} > 2$) indicate a large contribution of small particles, whereas small values (e.g.**
25 **$\text{SAE} < 1$) indicate a large contribution of large particles. SAE can be retrieved by remoting**
26 **sensing measurements and it serves as a proxy for particle size for satellite (e.g., Higurashi and**
27 **Nakajima, 1999; King et al., 1999; Liu et al., 2008) and sunphotometry (e.g., Holben et al.,**
28 **2001; Gobbi et al., 2007) retrieval of aerosol optical properties, even though it is well known**

1 that this is just a crude approximation. Many studies found that this relationship is not
2 unambiguous. Surface mean diameter (SMD) and volume mean diameter (VMD) correlate well
3 with SAE while geometric mean diameter (GMD) correlates poorly with SAE according to
4 Schuster et al. (2006), Virkkula et al. (2011) and Shen et al. (2018).

5
6 The reason for calculating both BSF and SAE in the present work is that they provide
7 information on the particle size distribution, yet being sensitive to slightly different particle size
8 ranges (e.g., Andrews et al., 2011; Collaud Coen et al., 2007). A detailed model analysis by
9 Collaud Coen et al., 2007) showed that BSF is more sensitive to small accumulation mode
10 particles, i.e., particles in the size range <400 nm whereas SAE is more sensitive to particles in
11 the size range of 500–800 nm.

13 **2.4 Light scattering calculated from the particle number size distributions**

14 Light scattering coefficients (both σ_{sp} and σ_{bsp}) were calculated using the Mie code similar to
15 Bohren and Huffman (1983). The refractive index was set to the average value of 1.517+0.019i
16 reported for SMEAR II by Virkkula et al. (2011). The wavelength for Mie modeling was set to
17 550 nm, which is the same as in the measurements. The whole size range of the DMPS or the
18 SMPS, depending on the station, was used. BSF was calculated from (1) by using the modeled
19 σ_{sp} and σ_{bsp} . Both the size range and the selected constant refractive index create uncertainty
20 especially when the modeled scattering is compared with scattering of PM10 aerosols. However,
21 the purpose of the modeled scattering was quality control and removal of inconsistent data.

23 **2.5 CCN number concentration calculated from the particle number size distribution**

24 The κ -Köhler theory uses a single parameter κ to describe the relationship between
25 hygroscopicity and water vapor saturation (Petters and Kreidenweis, 2007).

$$26 \quad S(D) = \frac{D^3 - D_d^3}{D^3 - D_d^3(1 - \kappa)} \exp\left(\frac{4\sigma_s/aM_w}{RT\rho_w D}\right) \quad (3)$$

27 Here $S(D)$ is water vapor saturation, which equals to SS+100%, D is the diameter of the wet
28 particle, D_d is particle dry diameter and κ is the hygroscopicity parameter. The rest of the

1 coefficients are usually set to constant, for instance in this study, $\sigma_{s/a} = 0.072 \text{ J/m}^2$ is the surface
 2 tension of the solution/air interface, $R = 8.314 \text{ J/mol}$ is the universal gas constant, $T = 298 \text{ K}$ is
 3 temperature, $\rho_w = 1000 \text{ kg/m}^3$ is the density of water, $M_w = 0.018 \text{ kg/mol}$ is the molecular weight
 4 of water. At given κ and D_d , $S(D)$ is a function of the wet diameter D , which is physically larger
 5 than D_d . As a combination of the Kelvin effect and the Raoult effect, $S(D)$ first increases and
 6 then decreases as D increases, and there is a maximum value for $S(D)$ in the S - D curve. Here,
 7 we call the maximum value of $S(D)$ and corresponding D as $S(D)_{\text{max}}$ and D_{max} respectively.
 8 Physically, if $S(D)_{\text{max}}$ larger than the SS of the environment, the dry particle will reach a wet
 9 diameter D between D_d and D_{max} ; while if $S(D)_{\text{max}}$ is smaller than the SS of the environment the
 10 dry particle can grow to infinite sizes, which means it is a so-called activated particle. $S(D)_{\text{max}}$
 11 decreases monotonically as D_d increases. Thus we can iterate D_d until $S(D)_{\text{max}}$ equals to a given
 12 SS. We call this D_d the critical diameter D_m . Particles with $D_d > D_m$ their $S(D)_{\text{max}} < \text{SS}$ and they
 13 can be activated while the smaller particles cannot.

14

15 Under the assumption of fully internally mixed particles, the CCN number concentration
 16 calculated from the particle number size distributions ($N_{\text{CCN}}(\text{PNSD})$) is obtained by integrating
 17 the PNSD of particles larger than the critical dry particle diameter (D_m):

$$18 \quad N_{\text{CCN}}(\text{PNSD}) = \int_{D_m}^{\infty} n(\log D_p) d \log D_p \quad (4)$$

19 at a given SS. All particles with a diameter larger than D_m can act as CCN. We calculated
 20 $N_{\text{CCN}}(\text{PNSD})$ at the supersaturations at which CCN were measured in the different stations (e.g.,
 21 0.1%, 0.2%, 0.3%, 0.5% and 1.0% for SMEAR II).

22

23 The accuracy of $N_{\text{CCN}}(\text{PNSD})$ is affected by the treatment of κ . In this study, we are not trying
 24 to achieve an accurate value of κ but instead want to illustrate that even an arbitrary setting of
 25 κ can yield reasonable CCN concentrations. This approach is named as ‘unknown chemical
 26 approach’ in (Kammermann et al., 2010) and as ‘Prediction of N_{CCN} from the constant κ ’ in
 27 Meng et al., (2014). Both of them give a detailed discussion of how this approach performs.
 28 Arbitrary κ is not performing as good as a proper κ when calculating N_{CCN} , yet we believe that
 29 it is good enough to be an alternative to measuring CCN in the empirical estimation of this

1 study. Wang et al. (2010) also claimed that $N_{\text{CCN}}(\text{PNSD})$ may be successfully obtained by
2 assuming an internal mixture and using bulk composition few hours after emissions. For
3 SORPES, ASI and PVC, we simply set a global-average value of 0.27 for κ (Pringle et al., 2010;
4 Kerminen et al., 2012). For the forest sites, SMEAR II and MAO, we set $\kappa = 0.12$, which is
5 close to the value of κ for Aitken mode particles reported previously by studies at forest sites
6 (Sihto et al., 2011; Hong et al., 2014). Here we used $N_{\text{CCN}}(\text{PNSD})$ for quality control and
7 removal of inconsistent data.

8 **2.6 Aerosol optical properties and CCN concentrations of simulated size distributions**

10 For studying the relationships of particle size, N_{CCN} and AOPs, we generated unimodal particle
11 number size distributions $n(\text{GMD}, \text{GSD})$ with varying the geometric mean diameter (GMD) and
12 geometric standard deviation (GSD). For them we calculated the same AOPs with the Mie
13 model as were obtained from the real measurements from the stations σ_{sp} and σ_{bsp} and from
14 these the BSF at the wavelengths $\lambda = 550$ nm. N_{CCN} was calculated simply by integrating
15 number concentrations of particles larger than a critical diameter of 50 nm, 80 nm, 90 nm, 100
16 nm, and 110 nm, and 150 nm. When the global average hygroscopicity parameter $\kappa = 0.27$ is
17 used this corresponds to a SS range of $\sim 0.14\% - 0.74\%$.

19 **Using a unimodal size distribution for the simulation is an approximation. In the boundary layer,**
20 **particle number size distributions consist typically of an Aitken mode in the size range of ~ 25**
21 **$- 100$ nm, an accumulation mode in the size range of $100 - 500$ nm and, following atmospheric**
22 **new particle formation, also a nucleation mode in the size range of < 25 nm (e.g., Dal Maso et**
23 **al., 2005; Herrmann et al., 2015; Qi et al., 2015). While the particle number concentration is**
24 **dominated by the smaller modes, essentially all light scattering is due to the accumulation mode**
25 **and also coarse particles in the range of $1 - 10$ μm . For example, at SMEAR II the average**
26 **contribution of particles smaller than 100 nm to total scattering was $\sim 0.2\%$ and even at the end**
27 **of new particle formation events it was no more than $\sim 2\%$ (Virkkula et al., 2011). Also most of**
28 **the CCN are in the accumulation mode size range, especially at low supersaturations ($\text{SS} <$**
29 **0.2%); at higher SS also Aitken mode particles contribute to CCN (Sihto et al., 2011).**

3. Relationships between N_{CCN} and AOPs

We first present general observations of the N_{CCN} and AOPs at all the six sites and investigate in more detail data from SMEAR II. Based on the relationships of AOPs and N_{CCN} at SMEAR II, we further use data from all the stations and develop a simple and general combined parameterization for estimating N_{CCN} .

3.1 Site-dependent N_{CCN} - AOP relationships

The averages of AOPs of PM_{10} particles and N_{CCN} at four supersaturations during the analyzed period for each site are presented in Table 2. In general all of them are cleaner than SORPES and more polluted than SMEAR II, based on the average values of σ_{sp} . The average values of N_{CCN} are obviously higher in more polluted air as well as can be seen in the values presented in Table 2. In all these different types of environments N_{CCN} apparently depends logarithmically on SS in the range $SS < 1.1\%$ (Fig 1). A power function $N_{CCN}(SS) = C \times (SS)^k$ was also fitted to the data, but it is obvious that the logarithmic function fits better to the data. Also the error function has been used to fit N_{CCN} vs. SS (e.g., Dusek et al., 2003 and 2006b). In the following analysis we will study how the dependence of N_{CCN} on supersaturation affects the relationships between N_{CCN} and AOPs.

Since there is obviously a positive correlation between the averages of N_{CCN} and σ_{sp} in Table 2, it is reasonable to study whether this is true also for the hourly-averaged data. A scatter plot shows that the correlation between N_{CCN} and σ_{sp} was weak at SMEAR II, especially for higher supersaturations (Fig 2). In spite of this, when the scatter plots are color-coded with respect to BSF, the relationship between N_{CCN} and σ_{sp} becomes clear: N_{CCN} grows almost linearly as a function of σ_{sp} for a narrow range of values of BSF. This indicates BSF can serve as a good proxy for describing the ratio between N_{CCN} and σ_{sp} .

Hereafter, we will use the term $R_{CCN/\sigma} = N_{CCN}/\sigma_{sp}$ to describe the relationship between N_{CCN} and σ_{sp} , similar to Liu and Li (2014). Note that this same ratio was defined as AR_{scat} in Tao et al. (2018). $R_{CCN/\sigma}$ varies over a wide range of values, so a proper parameterization to describe it is of significance.

1
2
3
4
5
6
7
8
9
10
11
12
13
14
15
16
17
18
19
20
21
22
23
24
25
26
27
28
29
30

The first step in the development of the parameterization was to calculate linear regressions of $R_{CCN/\sigma}$ vs BSF. $R_{CCN/\sigma}$ depends clearly on BSF (Fig. 3) as

$$R_{CCN/\sigma} = a \text{ BSF} + b \tag{5}$$

The correlation between BSF and $R_{CCN/\sigma}$ is strong when $\sigma_{sp} > 10 \text{ Mm}^{-1}$. At $\sigma_{sp} < 10 \text{ Mm}^{-1}$ the uncertainty of the nephelometer is higher, which may at least partly explain the lower correlation. Based on this we used $\sigma_{sp} > 10 \text{ Mm}^{-1}$ as the criterium for the data fitting.

Linear regressions of $R_{CCN/\sigma}$ vs BSF were applied to data from all the analyzed stations. For each dataset and individual supersaturation, a and b , i.e. the slope and offset of the linear regression, have different values as presented in Table 3. The calculation of a and b are based on data with $\sigma_{sp} > 10 \text{ Mm}^{-1}$ only. **The following discussion is based on the ordinary linear regression (OLR). In addition, we repeated the calculations with the Reduced Major Axis (RMA) regression, see supplement S2.**

The parameterization gives the formula for calculating $N_{CCN}(\text{AOP})$, i.e. N_{CCN} calculated from measurements of AOPs:

$$N_{CCN}(\text{AOP}_1) = (a_{ss}\text{BSF} + b_{ss}) \cdot \sigma_{sp} \tag{6}$$

The subscript 1 for AOP_1 indicates the first set of parameterization.

Scatter plots of $N_{CCN}(\text{AOP}_1)$ vs $N_{CCN}(\text{meas})$ are presented for two supersaturations, high and low, at the six stations (Fig. 4). The correlation coefficient R^2 between $N_{CCN}(\text{AOP}_1)$ and $N_{CCN}(\text{meas})$ is higher at lower supersaturations than that at higher supersaturations in most of the scatter plots shown in Fig. 4. A reasonable explanation for this is that the higher the supersaturation is, the smaller are the particles that can act as CCN. And further, the smaller the particles are, the less they contribute to both total scattering and backscattering and the higher is the relative uncertainty of both of them and thus also the uncertainty of $N_{CCN}(\text{AOP}_1)$.

3.2 Site-independent relationships between N_{CCN} , AOPs and supersaturations

The relationships between N_{CCN} and AOPs are obviously different for each site and

1 supersaturation. We next try to find a way to combine them into a site-independent form. First,
 2 the slopes and offsets obtained from the linear regression (Table 3) were plotted as a function
 3 of SS (Fig 5). The data obviously depend logarithmically on SS, so that (6) becomes

$$4 \quad N_{CCN}(AOP_2) = (a_{SS}BSF + b_{SS})\sigma_{sp} = ((a_1 \ln(SS) + a_0)BSF + b_1 \ln(SS) + b_0)\sigma_{sp} \quad (7)$$

5 The coefficients a_0 , a_1 , b_0 and b_1 obtained from the regression of $a_{SS} = a_1 \ln(SS) + a_0$ and $b_{SS} =$
 6 $b_1 \ln(SS) + b_0$ vs. the supersaturations SS for each station are presented in Table 4.

7
 8 Note that also a power function of SS of the form SS^k was used for fitting the data (Fig 5). This
 9 is the dependence on SS assumed for instance in the parameterization by Jefferson (2010). It is
 10 obvious that the power function fitting is not as good as the logarithm of SS. It has been
 11 observed that the error function describes well the SS dependence (e.g., Dusek et al., 2003;
 12 Dusek et al., 2006b), but in the SS range used in the present study the logarithm agrees well
 13 with the erf.

14
 15 The relationships of the coefficients in Table 4 are next used to get a combined, more general
 16 parameterization. Obviously the a_0 vs. a_1 , b_0 vs. b_1 , a_1 vs. b_1 and b_0 vs. b_1 pairs from all stations
 17 follow very accurately the same lines (Fig 6). Linear regressions yielding $a_0 = (2.38 \pm 0.06)a_1$,
 18 $b_0 = (2.33 \pm 0.03)b_1$, and $b_1 = (-0.096 \pm 0.013)a_1 + (6.0 \pm 5.9)$ were used, after the simple algebra
 19 in the supplement S3, to get

$$20 \quad N_{CCN}(AOP_2) \approx (\ln(SS) + (2.38 \pm 0.06))(a_1(BSF - (0.096 \pm 0.013)) + (6.0 \pm 5.9))\sigma_{sp}$$

$$21 \quad \approx \ln\left(\frac{SS}{0.093 \pm 0.006}\right)(a_1(BSF - (0.096 \pm 0.013)) + (6.0 \pm 5.9))\sigma_{sp} \quad (8)$$

22 where both the coefficient a_1 and the constant 6.0 ± 5.9 have units of $[N_{CCN}]/[\sigma_{sp}] = \text{cm}^{-3}/\text{Mm}^{-1}$.
 23 This is the general formula for the parameterization. In both (7) and (8) the only unquantified
 24 coefficient is now a_1 . However, we can find some ways to quantify also it.

25 For a given station, if there are simultaneous data of $N_{CCN}(\text{meas})$ and σ_{sp} for some reasonably
 26 long period, (8) can be adjusted. To estimate what is a reasonably long period, we added an
 27 analysis in the supplement S5. It shows that when the number of hourly samples is $> \sim 1000$,
 28 the uncertainty in BSF_{\min} is low enough. Instead of subtracting (0.096 ± 0.013) from BSF, the

1 minimum BSF = BSF_{\min} in the data set will be used. Further, when $BSF = BSF_{\min}$ the factor
 2 $a_1(BSF - BSF_{\min}) = 0$ and $N_{CCN}(AOP_2) \approx R_{\min} \cdot \sigma_{sp}$ where R_{\min} is the minimum $R_{CCN/\sigma}$ in the data
 3 set. It follows that

$$4 \quad N_{CCN}(AOP_2) \approx \left(a_1 \ln \left(\frac{SS}{0.093 \pm 0.006} \right) (BSF - BSF_{\min}) + R_{\min} \right) \sigma_{sp} \quad (9)$$

5 The derivation of (9) is shown in the supplement S4. In the data processing the 1st percentiles
 6 of both BSF and $R_{CCN/\sigma}$ are used as BSF_{\min} and R_{\min} , respectively. Here the free parameters are
 7 a_1 , BSF_{\min} and R_{\min} .

8

9 The coefficient a_1 is positively correlated with SAE. The linear regressions of a_1 and the average
 10 and median scattering Ångström exponent of PM_{10} particles (SAE) (Table 4) at the 6 sites in
 11 the analyzed periods yield $a_1 \approx (298 \pm 51)SAE \text{ cm}^{-3}/Mm^{-1}$ and $a_1 \approx (286 \pm 46)SAE \text{ cm}^{-3}/Mm^{-1}$,
 12 respectively (Fig. 7). The uncertainties are large, but the main point is that the correlations show
 13 that a_1 and thus $N_{CCN}(AOP_2)$ is higher for higher values of SAE. **If we consider the a_1 values in
 14 Table 4 as the accurate station-specific values, then using $a_1 = 286 \cdot SAE$ overestimates or
 15 underestimates a_1 by +37%, +30%, -20%, -32%, -20% and +251% for SMEAR II, SORPES,
 16 PGH, PVC, MAO and ASI, respectively. These values were calculated from $100\%(286 \cdot SAE -$
 17 $a_1)/a_1$. The effect of the biases of a_1 to the biases of $N_{CCN}(AOP_2)$ are discussed in more detail in
 18 the supplement S6. Nevertheless, we found that SAE is the only parameter that is positively
 19 correlated with a_1 and that can easily be obtained from nephelometer measurements. Searching
 20 for a more suitable proxy for a_1 would be an important part of follow up studies.**

21

22 R_{\min} of (9) was estimated by calculating the 1st percentile of $R_{CCN/\sigma}$ at each site at each SS. The
 23 average and standard deviation of R_{\min} was $5.2 \pm 3.3 \text{ cm}^{-3}/Mm^{-1}$. Consequently, the
 24 parameterization becomes

$$25 \quad N_{CCN}(AOP_2) \approx \left((286 \pm 46)SAE \cdot \ln \left(\frac{SS}{0.093 \pm 0.006} \right) (BSF - BSF_{\min}) + (5.2 \pm 3.3) \right) \sigma_{sp} \quad (10)$$

26 **The parameterization suggests that at any supersaturation and constant scattering coefficient,
 27 N_{CCN} is the higher the smaller the particles are because both SAE and BSF are roughly inversely
 28 correlated with the particle size. A qualitative explanation to this is that to keep σ_{sp} constant
 29 even if the dominating particle size decreases – which means that both SAE and BSF increase**

1 – the number of particles has to increase. The analysis also shows that neither SAE nor BSF
2 alone is enough for obtaining a good estimate of N_{CCN} from AOP measurements. This is again
3 in line with the model study of Collaud Coen et al. (2007) which showed that SAE and BSF are
4 sensitive to variations in somewhat different size ranges.

5
6 The parameterization in Eq (10) was applied to the data of the 6 stations and $N_{\text{CCN}}(\text{AOP}_2)$ was
7 compared with the $N_{\text{CCN}}(\text{meas})$ at the supersaturations used in the respective CCN counters.
8 The results are presented as scatter plots of $N_{\text{CCN}}(\text{AOP}_2)$ vs. $N_{\text{CCN}}(\text{meas})$ (Fig 8a and 8b), the
9 bias of the parameterization calculated as $N_{\text{CCN}}(\text{AOP}_2)/N_{\text{CCN}}(\text{meas})$ (Fig 8c) and the squared
10 correlation coefficient R^2 of the linear regression of $N_{\text{CCN}}(\text{AOP}_2)$ vs. $N_{\text{CCN}}(\text{meas})$ (Fig 8d). The
11 $N_{\text{CCN}}(\text{AOP}_2)$ values used for the statistics shown in Fig. 8 were calculated by using the SAE of
12 hourly-averaged scattering coefficients. The problem with that is that when $\text{SAE} < 0$ it is very
13 probable that also $N_{\text{CCN}}(\text{AOP}_2)$ is negative if $\text{BSF} > \text{BSF}_{\text{min}}$, as can be seen from Eq. (10). For
14 this reason the data with $\text{SAE} < 0$ were not used. The fraction of negative SAE hourly values
15 varied from 0.0% at SMEAR II and SORPES to 6% at MAO (Supplement S6, Table TS3). To
16 reduce the number of rejected data, we also calculated $N_{\text{CCN}}(\text{AOP}_2)$ by using the site-specific
17 median SAE shown in Table 4 and the hourly BSF values. The results are shown in the
18 supplement S6.

19
20 At the site-specific lowest values of SS, the scatter plots of $N_{\text{CCN}}(\text{AOP}_2)$ vs. $N_{\text{CCN}}(\text{meas})$ of data
21 from most stations clustered along the 1:1 line, but for the Himalayan site PGH the
22 parameterization yielded significantly higher concentrations (Fig 8a). The bias varied from 0.7
23 to > 4 (Fig 8c) (Table TS3). At PGH at the lowest SS, the bias was > 4 but decreased to ~ 1.1 -
24 1.2 at $\text{SS} = 0.4\%$ and even closer to 1 at higher SS. At $\text{SS} > 0.4\%$, the average bias varied
25 between ~ 0.7 and ~ 1.3 , which means N_{CCN} was estimated with an average uncertainty of
26 approximately 30% by using nephelometer data. For ASI the bias was higher, in the range of
27 $\sim 1.4 - 1.9$. For the US coastal site PVC, the parameterization constantly underestimated the
28 CCN concentrations by about 30%. Since $N_{\text{CCN}}(\text{AOP}_2) \approx (a_j \ln(\text{SS}/0.093)(\text{BSF} - \text{BSF}_{\text{min}}) +$
29 $R_{\text{min}})\sigma_{\text{sp}}$, it is obvious that biases of a_j affect the bias of $N_{\text{CCN}}(\text{AOP}_2)$. As it was written above,

1 the parameterization of $a_1 = 286 \cdot \text{SAE}$ overestimates or underestimates a_1 . For most stations the
2 bias of $N_{\text{CCN}}(\text{AOP}_2)$ can be explained by the bias of a_1 : when a_1 is underestimated so is
3 $N_{\text{CCN}}(\text{AOP}_2)$, and when a_1 is overestimated so is $N_{\text{CCN}}(\text{AOP}_2)$. A detailed analysis of the effect
4 of the bias of a_1 on the bias of $N_{\text{CCN}}(\text{AOP}_2)$ is presented in the supplement S6.

5
6 The correlation coefficient of $N_{\text{CCN}}(\text{AOP}_2)$ vs. $N_{\text{CCN}}(\text{meas})$ is higher at higher CCN
7 concentrations (not shown in the figure). One possible reason for this is that when CCN
8 concentration is lower, the aerosol loading is usually lower and also the relative uncertainties
9 of both N_{CCN} and AOPs are higher than at high concentrations.

11 **4. Analyses of size distribution effects on N_{CCN} –AOP relationships**

12 Below we will first present effects of simulated size distributions on the relationships between
13 N_{CCN} and aerosol optical properties and then compare the simulations with field data.

15 **4.1 N_{CCN} –AOP relationships of simulated particle size distributions**

16 We generated lognormal unimodal size distributions as explained in section 2.6. GMD was
17 given logarithmically evenly-spaced values from 50 nm to 1600 nm and GSD was given two
18 values: 1.5 representing a relatively narrow size distribution and 2.0 a wide size distribution.
19 We then calculated AOPs, N_{CCN} and $R_{\text{CCN}/\sigma}$ for these size distributions.

20
21 The reasoning for the approach of estimating N_{CCN} from σ_{sp} and BSF can easily be explained
22 by the qualitatively similar variations of $R_{\text{CCN}/\sigma}$ and BSF as function of GMD (Fig. 9). $R_{\text{CCN}/\sigma}$ is
23 the highest for the smallest particles, i.e. for GMD = 50 nm and it decreases with an increasing
24 GMD as also BSF. Note that the width of the size distribution has very strong effects on $R_{\text{CCN}/\sigma}$:
25 for the wide size distribution it is approximately an order of magnitude lower than for the
26 narrow size distribution. Note also that the values of $R_{\text{CCN}/\sigma}$ of the wide size distributions are
27 plotted twice (Fig. 9a): the black symbols and line use the left axis to emphasize the big
28 difference in the magnitudes of the wide and narrow size distributions; the red symbols and line
29 use the right axis to show that the shape of the $R_{\text{CCN}/\sigma}$ size distribution is very similar to the one
30 calculated for the narrow size distributions. The simulation also shows a potential source of

1 uncertainty of the method: in the GMD range of ~500 – 800 nm, the BSF of the narrow size
2 distribution actually increases, although very little with an increasing value of GMD (Fig. 9b).
3 This phenomenon is due to Mie scattering and it is even stronger for single particles. When the
4 size parameter $x = \pi D_p / \lambda$ of non-absorbing and weakly-absorbing spherical particles grows
5 from ~3 to ~8, their BSF increases and then decreases again as can be shown by Mie modeling
6 (Wiscombe and Grams, 1976). For the wavelength $\lambda = 550$ nm this corresponds to a particle
7 diameter range of ~525 to ~1400 nm.

8
9 The decrease of $R_{CCN/\sigma}$ and BSF with the increasing GMD was used for estimating particle sizes
10 with a stepwise linear regression. An example is given by the linear regressions of $R_{CCN/\sigma}$ vs.
11 BSF calculated for 5 consecutive size distributions, first for those that have their GMDs from
12 50 nm to 100 nm and the second for those that have their GMDs from 100 nm to 200 nm (Fig.
13 10). Note that it is obvious that linear regressions are applicable for short intervals but not well
14 for the whole size range. It is also obvious that an exponential fit would be perfect to explain
15 the relationship between $R_{CCN/\sigma}$ and BSF. But this is not what we are looking for. We are
16 looking for the slopes and offsets in the relationship $R_{CCN/\sigma} = aBSF + b$ that was used for fitting
17 the field measurement data. So, physically it would mean that N_{CCN} would increase linearly as
18 a function of BSF even though this is not exactly correct.

19
20 The absolute values of the slopes and offsets are clearly lower for the larger particle size range.
21 Here, we define the particle size used for describing the size range of each regression as the
22 equivalent geometric mean diameter GMD_e , the geometric mean of the range of the GMDs of
23 the unimodal size distributions used for each regression. In other words,
24 $GMD_e = \sqrt{GMD_{low} GMD_{high}}$, where GMD_{low} and GMD_{high} are the smallest GMD and the largest
25 GMD of the range, respectively. Two examples of the regressions were given above, one
26 calculated for the GMD range from 50 nm to 100 nm and the other for the GMD range from
27 100 nm to 200 nm. The GMD_e s of these two size ranges are 70.7 nm and 141.4 nm, respectively.
28 It will be shown below that GMD_e is a mathematical concept that helps to explain the observed
29 relationships, not an actual GMD of the particle size distribution at the sites.

1
2
3
4
5
6
7
8
9
10
11
12
13
14
15
16
17
18
19
20
21
22
23
24
25
26
27
28
29
30

For a wide size distribution, the slopes and offsets of the regressions of $R_{CCN/\sigma}$ vs. BSF decrease and increase, respectively, monotonically with an increasing value of GMD_e in the whole size range studied here (Fig. 11). For a narrow size distribution, the slope decreases until $GMD_e \approx 300$ nm and then increases, which means that there is no unambiguous relationship between them. The reason is, as discussed above related to Fig 9b, that in the GMD range of $\sim 500 - 800$ nm the BSF of narrow size distributions increases slightly with an increasing GMD.

Note also that the ranges of the absolute values of the slopes and offsets of the narrow and wide size distributions are very different. For instance, when $GMD_e = 100$ nm the slope $a \approx 4000$ cm^{-3}/Mm^{-1} and $a \approx 1600$ cm^{-3}/Mm^{-1} for the narrow and wide size distribution, respectively. Since $N_{CCN}(AOP) = R_{CCN/\sigma} \cdot \sigma_{sp} = (aBSF + b)\sigma_{sp}$ this means that the $N_{CCN}(AOP)$ of narrow size distributions is more sensitive to variations in mean particle size than the $N_{CCN}(AOP)$ of wide size distributions.

We plotted the offset vs. slope of the unimodal size distributions and those obtained from the linear regressions of the field data at the supersaturations presented in Table 3 and below it the GMD_e vs. the slopes of the regressions of the unimodal size distributions (Fig 12). In Fig. 12 also the effect of the choice of the activation diameters of 50 nm, 80 nm, 110 nm, and 150 nm is shown.

Several observations can be made in Fig. 12. First, for the simulated wide size distributions the relationship between the offset and slope is unambiguous, while this is not the case for the narrow size distributions at sizes $GMD_e > \sim 200$ nm (Fig 12b). Second, the field data points roughly follow the lines of the simulations. This suggests that the slopes and offsets of the linear regressions of $R_{CCN/\sigma}$ vs. BSF yield information on the dominating particle sizes just as they do for the simulated size distributions. For instance, the PVC data point corresponding to the highest supersaturation has the highest slope (1970 cm^{-3}/Mm^{-3} , Table 3) and it is close to the wide size distribution line with the activation diameter of 50 nm (Fig. 12a). This corresponds to the GMD_e of ~ 150 nm (Fig. 12b). The SMEAR II high SS offset vs. slope fits best with the

1 corresponding lines of the narrow unimodal size distributions with activation diameters in the
2 range of ~50 – 110 nm and the corresponding $GMD_e \approx 150 - 200$ nm.

3
4 At the lowest SS, the offset vs. slope points of all stations agree well with the lines derived from
5 the unimodal modes. This is actually in line with the higher correlation coefficients (R^2) of the
6 regressions of N_{CCN} (AOP_1) vs. N_{CCN} (meas) at the lowest SS (Fig. 4). This can be explained by
7 that at low SS small particles do not get activated and unimodal size distributions in the
8 accumulation mode are mainly responsible for CCN. For ASI the slopes and offsets of the
9 lowest and highest SS are especially close to each other, closer than at any other station (Fig.
10 12a), and the corresponding $GMD_e \approx 750$ nm and 400 nm, respectively, when the GMD_e vs. a
11 relationship of any of the distributions is used (Fig. 12b). This is in line with that ASI is an
12 island site dominated by marine aerosols. For PGH at the lowest SS, the slope is actually
13 negative which is not obtained from the simulations at all so no GMD_e can be given for it.

14 15 **4.2 Aerosol size characteristics of the sites**

16 As it was shown above, particle size distributions affect the relationships between N_{CCN} and
17 AOPs. It is therefore discussed here how the size distributions vary at the six sites of the study
18 and whether they support the interpretations presented above. The size distributions are
19 discussed using the particle number size distribution data and the ratios of σ_{sp} of PM_{10} and $PM_{2.5}$
20 size ranges from those stations where they are available.

21 22 **4.2.1 Diurnal variation of particle number size distribution**

23 Fig. 13a shows the averaged diurnal cycle of PNSD at the sites where either a DMPS or SMPS
24 is available. New particle formation (NPF) events are a significant source of uncertainty in the
25 prediction of N_{CCN} (Kerminen et al., 2012; Ma et al., 2016). Complete NPF events start from a
26 burst of sub-10 nm particles followed by a continuous growth up to a few hundred nanometers.
27 As a result, the size distribution varies significantly. NPF is one possible explanation of the
28 poor N_{CCN} - σ_{sp} correlation.

29
30 SMEAR II and SORPES are reported to have an appreciable frequency of NPF (Kulmala et al.,

1 2004; Dal Maso et al., 2005; Sihto et al., 2006; Qi et al., 2015). A continuous growth of particle
2 size at SORPES can usually last for several days after NPF (Shen et al. 2018). Similar growth
3 patterns have also been observed in the Two-Column Aerosol Project (TCAP;
4 <http://campaign.arm.gov/tcap/>; refers as PVC in this study) according to Kassianov et al. (2014).
5 NPF is rarely observed in the Amazon forest, as reported by Wang et al. (2016). However, it
6 does take place at MAO as is shown in the diurnal cycle of PNSD. The reason is probably that
7 the MAO site was measuring aerosol downwind of the City Manaus. At ASI, there no evidence
8 of NPF according to the PNSD diurnal cycle.

9

10 These observations of the NPF are compared with the bias and correlation coefficients of the
11 parameterization discussed in section 4.1 (Fig. 8). The correlation coefficient of $N_{CCN}(AOP_2)$
12 vs. $N_{CCN}(meas)$ is the highest, $R^2 > 0.85$ at all SS at ASI where no NPF takes place and clearly
13 lower at the other sites (Fig 8d). For the bias NPF appears not to have a clear influence: for both
14 SMEAR II and SORPES bias varies from ~1.1 to ~1.4 at $SS > 0.1\%$. **As it was stated above**
15 **(section 3.2), for most stations the bias of $N_{CCN}(AOP_2)$ can be explained by the bias of a_1 in**
16 **$N_{CCN}(AOP_2) \approx (a_1 \ln(SS/0.093))(BSF - BSF_{min}) + R_{min})\sigma_{sp}$.**

17

18 **4.2.2 Distributions of geometric mean diameters**

19 Figure 13b presents the normalized distributions of the geometric mean diameters at SMEAR
20 II, SORPES, PVC, MAO and ASI. They vary from 20 nm to 200 nm at all sites, with the most
21 frequent GMD between ~70 nm and ~120 nm depending on the site. This shows clearly that
22 the above-presented equivalent geometric mean diameter GMD_e calculated assuming a
23 unimodal size distribution is not a quantitative GMD of the size distribution, it is a mathematical
24 concept that explains partially the relationships of $R_{CCN/\sigma}$ and BSF. **However, the GMD of the**
25 **measured size distribution and GMD_e are not quite comparable also for another reason. The**
26 **simulations were made by using unimodal size distributions, so that GMD_e varied in the range**
27 **70 nm – 1100 nm (Fig. 11) while the GMDs were calculated from DMPS and SMPS data that**
28 **also contained the nucleation and Aitken modes that often dominate the total particle number**
29 **concentration.**

30

1 The frequency distribution of GMD at SMEAR II is the widest among the five sites with PNSD
2 data available, followed by SORPES and PVC. At MAO the frequency distribution of GMD
3 has two peaks in this study. The lower peak is possibly due to the burst of sub-20 nm particles,
4 since these these particles have little chance to grow to sizes where they can serve as CCN. The
5 second peak at around 100 nm possibly represents the GMD without the burst of sub-20 nm
6 particles and it is distinctly narrower than at SMEAR II, SORPES and PVC.

7

8 A comparison of the correlation coefficients of N_{CCN} (AOP₂) vs. N_{CCN} (meas) (Fig. 8d) and the
9 widths of the GMD frequency distributions (Fig. 13b) do not show any clear relationships,
10 except in ASI. The frequency distribution of GMD is the narrowest at ASI, indicating that the
11 average particle size does not change much throughout the whole period. This is in line with
12 the low variation of the slope and offset of the R_{CCN} vs BSF of ASI (Fig 12a). At ASI also the
13 correlation coefficient of N_{CCN} (AOP₂) vs. N_{CCN} (meas) is the highest, $R^2 \approx 0.8$ at all SS.

14

15 **4.3.3 Contribution of light scattering by sub- μ m particles**

16 There is one more measure related to particle size distribution, the ratio between σ_{sp} of sub-1
17 μ m and sub-10 μ m aerosol ($\sigma_{sp}(PM_1)/\sigma_{sp}(PM_{10})$). At SMEAR II, the contribution of submicron
18 particles usually varies within a range of $\sim 0.8\sim 0.9$ and it is the highest among all sites in this
19 study. PVC has two peaks in the $\sigma_{sp}(PM_1)/\sigma_{sp}(PM_{10})$ distribution, the peak around 0.2
20 corresponding to air masses from the sea, with a very low scattering coefficient and N_{CCN} . By
21 ignoring the cleanest air masses ($\sigma_{sp} < 5 \text{ Mm}^{-1}$), the fraction of $\sigma_{sp}(PM_1)/\sigma_{sp}(PM_{10})$ is usually
22 around 0.8, which is just slightly lower than at SMEAR II. At PGH and MAO, the distribution
23 of the ratio is wider, and the peak position is at about 0.65. The overall contribution of sub- μ m
24 particle light scattering at PGH is moderate among the sites in this study. At ASI,
25 $\sigma_{sp}(PM_1)/\sigma_{sp}(PM_{10})$ is the lowest among all sites in this study, indicating that particles larger
26 than 1 μ m contribute a considerable fraction of total light scattering. For SORPES
27 $\sigma_{sp}(PM_1)/\sigma_{sp}(PM_{10})$ is not available.

28

29 Among those five sites, when $\sigma_{sp}(PM_1)/\sigma_{sp}(PM_{10})$ decreases, the correlation between BSF and

1 $R_{CCN/\sigma}$ decreases (not shown in a scatter plot). At some sites (e.g., ASI) the BSF of PM_{10} is often
2 even larger than that of PM_1 , which can be an error in the measurements but it may also be due
3 to a real phenomenon. As discussed in section 4.1, for single spherical particles Mie modeling
4 shows that in the particle diameter range of ~525 to ~1400 nm BSF increases with an increasing
5 D_p . Mugnai and Wiscombe (1986) simulated scattering by non-spherical particles and found
6 that BSF increases when the size parameter x grows from ~8 to ~15, which corresponds to the
7 particle diameter range of ~1400 nm to ~2600 nm at $\lambda = 550$ nm. Therefore it is obvious that
8 large and non-spherical particles like sea salt and dust will blur the correlation between BSF
9 and $R_{CCN/\sigma}$. In such a case the increase in the amount of large particles sometimes leads to an
10 increase of BSF and a decrease of $R_{CCN/\sigma}$, which is opposite to the usual positive correlation
11 between BSF and $R_{CCN/\sigma}$ in this study. This may be at least part of the explanation of the highest
12 bias at high values of SS in ASI (Fig 8c), the site dominated by marine aerosol. Thus, the lower
13 $\sigma_{sp}(PM_1)/\sigma_{sp}(PM_{10})$ may in principle result in a poor performance of our method. However, a
14 comparison of the correlation coefficients and the $\sigma_{sp}(PM_1)/\sigma_{sp}(PM_{10})$ frequency distributions
15 of each site shows the opposite. At the highest SS of each site, the R^2 in a decreasing order is
16 ASI, PGH, MAO, SORPES, SMEAR II, and PVC (Fig. 8d). The peaks, i.e. modes of the
17 frequency distribution of $\sigma_{sp}(PM_1)/\sigma_{sp}(PM_{10})$ are, in a growing order, ASI: 0.375, PGH: 0.625,
18 MAO: 0.65, PVC: 0.825, SMEAR II: 0.875. Note that at SORPES there is only one size range
19 measured. Of these the R^2 of only PVC and SMEAR II are not in the same order (Fig 8d). This
20 suggests that N_{CCN} can be estimated better from the aerosol optical properties for sites
21 dominated by large particles than for sites dominated by small particles. This further suggests
22 that the ambient size distributions were so wide that the non-monotonous relationship between
23 particle size and BSF discussed above did not play an important role. On the other hand, the
24 bias at the highest SS has no clear relationship with $\sigma_{sp}(PM_1)/\sigma_{sp}(PM_{10})$. .

25

26 There is also an additional observation that can be made. The above-mentioned order of the
27 modes of the frequency distribution of $\sigma_{sp}(PM_1)/\sigma_{sp}(PM_{10})$ is almost the same as the order of
28 the slopes and offsets and GMD_{eS} in Fig. 12. Only for SMEAR II and PVC the order is not the
29 same. This further supports the interpretation that the slopes and offsets of the linear regression
30 of R_{CCN} vs BSF depend on the dominating particle size of particle size distribution.

5. Conclusions

The relationships between aerosol optical properties, CCN number concentrations (N_{CCN}) and particle number size distributions were investigated based on in-situ measurement data from six stations in very different environments around the world. The goals were to find physical explanations of the relationships and to find a parametrization to obtain N_{CCN} from sites where AOPs are measured but no CCN counter is available. There are many previous parameterizations for doing just the same. As a starting point we used the parameterization presented by Jefferson (2010). That one needs also absorption measurements since it includes single-scattering albedo. We instead studied how the parameterization would look like if only total scattering and backscattering data were available.

The basic idea for the parameterization is that N_{CCN} is proportional to σ_{sp} and a function of the backscatter fraction (BSF), i.e., $N_{\text{CCN}}(\text{AOP}) = (a\text{BSF} + b)\sigma_{\text{sp}}$ as is also in the parameterization of Jefferson (2010). In the study of the physical explanation of the relationships between N_{CCN} and AOPs, we found that the slope a and offset b in $N_{\text{CCN}}(\text{AOP}) = (a\text{BSF} + b)\sigma_{\text{sp}}$ depend clearly on the dominating particle size and on the width of the size distributions. This was shown first by simulations and then by comparisons of the simulations with field data. The analyses showed that the sensitivity of $N_{\text{CCN}}(\text{AOP})$ to variations of BSF increases with a decreasing particle size. As a result, sites dominated by supermicron aerosol particles, such as ASI that is dominated by marine aerosol, have a small value of the slope a in the above formula, which means that it is not very sensitive to variations in BSF. Sites dominated by small aerosol particles are clearly more sensitive. For instance for the coastal site PVC that is significantly affected by anthropogenic emissions, the slope a in the above formula is an order of magnitude higher than at the marine site.

The dependence on supersaturation proved to be logarithmic, different from that of Jefferson (2010). We first showed that for the average N_{CCN} measured with CCN counters at supersaturations ranging from 0.1% to 1.1%. For $N_{\text{CCN}}(\text{AOP})$ we also got a logarithmic dependence on SS : $N_{\text{CCN}}(\text{AOP}) \approx (286\text{SAE} \cdot \ln(SS/0.093)(\text{BSF} - \text{BSF}_{\text{min}}) + (5.2 \pm 3.3))\sigma_{\text{sp}}$. Actually this result is qualitatively in line with the relationship between AOD and CCN reported

1 by Andreae (2010). The derived $N_{CCN}(AOP)$ depends on σ_{sp} , SAE and BSF. The analysis shows
2 that neither SAE nor BSF alone is enough for obtaining a good estimate of N_{CCN} from AOP
3 measurements.

4
5 At the lowest supersaturations of each site ($SS \approx 0.1\%$), the average bias, defined as the ratio
6 of the AOP-derived and measured N_{CCN} , varied from ~ 0.7 to ~ 1.9 at most sites except at the
7 Himalayan site PGH where the bias was > 4 . At $SS > 0.4\%$ the average bias ranged from ~ 0.7
8 to ~ 1.3 at most sites. For the marine-aerosol dominated site ASI the bias was higher, $\sim 1.4 - 1.9$.
9 In other words, at $SS > 0.3\%$ N_{CCN} was estimated with an average uncertainty of approximately
10 30% by using nephelometer data. The biases were mainly due to the biases in the
11 parameterization related to the scattering Ångström exponent SAE.

14 **Author contributions**

15 YS carried out measurements at SORPES in China, analyzed and visualized data of all sites,
16 and wrote the original draft. AV contributed to data analysis and visualization, writing and
17 editing the original draft, and supervised the work of YS in Finland. AD provided funding for
18 the measurements and research at SORPES in China, acquired funding for YS in China, and
19 supervised the work of YS. KL, HK and PA carried out measurements, data collection and
20 maintenance of measurement data of SMEAR II in Finland. YS, XC, XQ, WN and XH carried
21 out measurements, data collection and maintenance of measurement data of SORPES in China.
22 MK and TP provided the funding for YS in Finland. MK provided funding for the
23 measurements and research at SMEAR II in Finland. TP and VMK formulated the goals of the
24 research and supervised it.

26 **Acknowledgments**

27 This work was supported by National Natural Science Foundation of China (41725020),
28 Academy of Finland via Center of Excellence in Atmospheric Sciences (project no. 272041),
29 the Centre for International Mobility CIMO of the Finnish Government Scholarship Pool
30 programme, and the Collaborative Innovation Center of Climate Change supported by the

1 Jiangsu 2011 Program. Data were also obtained from the Atmospheric Radiation Measurement
2 (ARM) User Facility, a U.S. Department of Energy (DOE) Office of Science user facility
3 managed by the Office of Biological and Environmental Research. For the SMEAR II data we
4 thank the SMEAR II technical team. Y. Shen was supported by the CSC-Finnish joint PhD
5 studentship.

6

7 **References**

8 Aalto, P., Hämeri, K., Becker, E., Weber, R., Salm, J., Mäkelä, J., Hoell, C., O’ Dowd, C.,
9 Hansson, H.-C., Väkevä, M., Koponen, I., Buzorius, G., and Kulmala, M.: Physical
10 characterization of aerosol particles during nucleation events, *Tellus B*, 53, 344–358,
11 <https://doi.org/10.3402/tellusb.v53i4.17127>, 2001.

12

13 Andreae, M. O.: Correlation between cloud condensation nuclei concentration and aerosol
14 optical thickness in remote and polluted regions, *Atmos. Chem. Phys.*, 9, 543–556,
15 <https://doi.org/10.5194/acp-9-543-2009>, 2009.

16

17 **Andrews, E., Ogren, J. A., Bonasoni, P., Marinoni, A., Cuevas, E., Rodríguez, S., Sun, J. Y.,**
18 **Jaffe, D. A., Fischer, E. V., Baltensperger, U., and Weingartner, E.: Climatology of aerosol**
19 **radiative properties in the free troposphere, *Atmos. Res.*, 102, 365–393, 2011.**

20

21 Berg, L. K., Fast, J. D., Barnard, J. C., Burton, S. P., Cairns, B., Chand, D., Comstock, J. M.,
22 Dunagan, S., Ferrare, R. A., Flynn, C. J., Hair, J. W., Hostetler, C. A., Hubbe J., Jefferson, A.,
23 Johnson, R., Kassianov, E. I., Kluzek, C. D., Kollias, P., Lamer, K., Lantz, K., Mei, F., Miller,
24 M. A., Michalsky, J., Ortega, I., Pekour, M., Rogers, R. R., Russell, P. B., Redemann, J.,
25 Sedlacek III, A. J., Segal-Rosenheimer, M., Schmid, B., Shilling, J. E., Shinozuka, Y.,
26 Springston, S. R., Tomlinson, J. M., Tyrrell, M., Wilson, J. M., Volkamer, R., Zelenyuk, A., and
27 Berkowitz, C. M.: The Two-Column Aerosol Project: Phase I – Overview and impact of
28 elevated aerosol layers on aerosol optical depth, *J. Geophys. Res.-Atmos.*, 121, 336–361, 2016.

29

30 Bohren, C. F. and Huffman, D. R.: Absorption and scattering of light by small particles, 1st ed.

1 Wiley, New York, 57–81, 1983.

2

3 Cantrell, C. A.: Technical Note: Review of methods for linear leastsquares fitting of data and
4 application to atmospheric chemistry problems, *Atmos. Chem. Phys.*, 8, 5477–5487,
5 doi:10.5194/acp-8-5477-2008, 2008.

6

7 Collaud Coen, M., Weingartner, E., Nyeki, S., Cozic, J., Henning, S., Verheggen, B., Gehrig,
8 R., and Baltensperger, U.: Long-term trend analysis of aerosol variables at the high alpine site
9 Jungfraujoch, *J. Geophys. Res.* 112,D13213. <https://doi.org/10.1029/2006JD007995>, 2007.

10

11 Crosbie, E., Youn, J.-S., Balch, B., Wonaschütz, A., Shingler, T., Wang, Z., Conant, W. C.,
12 Betterton, E. A., and Sorooshian, A.: On the competition among aerosol number, size and
13 composition in predicting CCN variability: a multi-annual field study in an urbanized desert,
14 *Atmos. Chem. Phys.*, 15, 6943–6958, <https://doi.org/10.5194/acp-15-6943-2015>, 2015.

15

16 Dal Maso, M., Kulmala, M., Riipinen, I., Wagner, R., Hussein, T., Aalto, P. P., and Lehtinen, K.
17 E. J.: Formation and growth of fresh atmospheric aerosols: eight years of aerosol size
18 distribution data from SMEAR II, Hyytiälä, Finland, *Boreal Environ. Res.*, 10, 323–336, 2005

19

20 de Sá, S. S., Rizzo, L. V., Palm, B. B., Campuzano-Jost, P., Day, D. A., Yee, L. D., Wernis, R.,
21 Isaacman-VanWertz, G., Brito, J., Carbone, S., Liu, Y. J., Sedlacek, A., Springston, S.,
22 Goldstein, A. H., Barbosa, H. M. J., Alexander, M. L., Artaxo, P., Jimenez, J. L., and Martin, S.
23 T.: Contributions of biomass-burning, urban, and biogenic emissions to the concentrations and
24 light-absorbing properties of particulate matter in central Amazonia during the dry season,
25 *Atmos. Chem. Phys.*, 19, 7973–8001, <https://doi.org/10.5194/acp-19-7973-2019>, 2019.

26

27 Ding, A. J., Fu, C. B., Yang, X. Q., Sun, J. N., Zheng, L. F., Xie, Y. N., Herrmann, E., Nie, W.,
28 Petäjä, T., Kerminen, V.-M., and Kulmala, M.: Ozone and fine particle in the western Yangtze
29 River Delta: an overview of 1 yr data at the SORPES station, *Atmos. Chem. Phys.*, 13, 5813–
30 5830, doi:10.5194/acp-13-5813-2013, 2013.

1
2
3
4
5
6
7
8
9
10
11
12
13
14
15
16
17
18
19
20
21
22
23
24
25
26
27
28
29
30

Ding, A. J., Nie, W., Huang, X., Chi, X., Sun, J., Kerminen, V. M., Xu, Z., Guo, W., Petaja, T., Yang, X. Q., Kulmala, M., and Fu, C.: Long-term observation of air pollution-weather/climate interactions at the SORPES station: A review and outlook, *Front. Environ. Sci. Eng.*, 10, doi:10.1007/s11783-016-0877-3, online first, 2016.

DMT: Cloud Condensation Nuclei Counter Operator Manual, DOC-0086 Rev G-1, Droplet Measurement Technologies, Inc., p. 107, 2009.

Dusek, U., Covert, D. S., Wiedensohler, A., Neususs, C., Weise, D., and Cantrell, W.: Cloud condensation nuclei spectra derived from size distributions and hygroscopic properties of the aerosol in coastal south-west Portugal during ACE-2, *Tellus Series B –Chemical and Physical Meteorology*, 55, 35–53, 2003.

Dusek, U., Frank, G. P., Hildebrandt, L, Curtius, J., Schneider, J., Walter, S., Chand, D., Drewnick, F., Hings, S., Jung, D., Bormann, S., and Andreae, M. O.: Size matters more than chemistry for cloud-nucleating ability of aerosol particles, *Science*, 312, 1375–1378, 2006a.

Dusek, U., Reischl, G. P., and Hitzenberger, R.: CCN activation of pure and coated carbon black particles, *Environ. Sci. Technol.*, 40, 1223–1230, 2006b.

Ervens, B., Cubison, M., Andrews, E., Feingold, G., Ogren, J. A., Jimenez, J. L., DeCarlo, P., and Nenes, A.: Prediction of cloud condensation nucleus number concentration using measurements of aerosol size distributions and composition and light scattering enhancement due to humidity, *J. Geophys. Res.-Atmos.*, 112, D10S32, <https://doi.org/10.1029/2006jd007426>, 2007.

Forster, P., Ramaswamy, V., Artaxo, P., Berntsen, T., Betts, R., Fahey, D. W., Haywood, J., Lean, J., Lowe, D. C., Myhre, G., Nganga, J., Prinn, R., Raga, G., Schulz, M., and Van Dorland, R.: Changes in Atmospheric Constituents and in Radiative Forcing, in: *Climate Change 2007: The*

1 Physical Science Basis, contribution of Working Group I to the Fourth Assessment Report of
2 the Intergovernmental Panel on Climate Change, edited by: Solomon, S. D., Qin, M., Manning,
3 Z., Chen, M., Marquis, K. B., Averyt, M. T., and Miller, H. L., Cambridge University Press,
4 Cambridge, United Kingdom and New York, NY, USA, 129– 134, 2007.

5

6 Ghan, S. J., Rissman, T. A., Elleman, R., Ferrare, R. A., Turner, D., Flynn, C., Wang, J., Ogren,
7 J., Hudson, J., Jonsson, H. H., VanReken, T., Flagan, R. C., and Seinfeld, J. H.: Use of in situ
8 cloud condensation nuclei, extinction, and aerosol size distribution measurements to test a
9 method for retrieving cloud condensation nuclei profiles from surface measurements, *J.*
10 *Geophys. Res.- Atmos.*, 111, D05s10, <https://doi.org/10.1029/2004jd005752>, 2006.

11

12 Gobbi, G. P., Kaufman, Y. J., Koren, I., and Eck, T. F.: Classification of aerosol properties
13 derived from AERONET direct sun data, *Atmos. Chem. Phys.*, 7, 453–458, doi:10.5194/acp-7-
14 453-2007, 2007.

15

16 Gogoi, M. M., S. S. Babu, V. Jayachandran, K. K. Moorthy, S. K. Satheesh, M. Naja, and V.
17 R. Kotamarthi (2015), Optical properties and CCN activity of aerosols in a high-altitude
18 Himalayan environment: Results from RAWEX-GVAX, *J. Geophys. Res. Atmos.*, 120, 2453–
19 2469, doi:10.1002/2014JD022966.

20

21 Herrmann, E., Weingartner, E., Henne, S., Vuilleumier, L., Bukowiecki,
22 N., Steinbacher, M., Conen, F., Collaud Coen, M., Hammer, E., Jurányi, Z., Baltensperger, U.,
23 and Gysel, M.: Analysis of long-term aerosol size distribution data from Jungfraujoch with
24 emphasis on free tropospheric conditions, cloud influence, and air mass
25 transport, *J. Geophys. Res.-Atmos.*, 120,9459-9480, doi:10.1002/2015JD023660, 2015.

26

27 Higurashi, A. and Nakajima, T.: Development of a Two-Channel Aerosol Retrieval Algorithm
28 on a Global Scale Using NOAA AVHRR, *J. Atmos. Sci.*, 56, 924–941, 1999.

29

30 Holben, B. N., Tanré, D., Smirnov, A., Eck, T. F., Slutsker, I., Abuhassan, N., Newcomb, W.

1 W., Schafer, J. S., Chatenet, B., Lavenu, F., Kaufman, Y. J., Castle, J. V., Setzer, A., Markham,
2 B., Frouin, D. C. R., Halthore, R., Karneli, A., O'Neill, N. T., Pietras, C., Pinker, R. T., Voss,
3 K., and Zibordi, G.: An emerging ground-based aerosol climatology: Aerosol optical depth
4 from AERONET, *J. Geophys. Res.*, 106, 12067–12098, 2001.

5
6 Hong, J., Häkkinen, S. A. K., Paramonov, M., Äijälä, M., Hakala, J., Nieminen, T., Mikkilä, J.,
7 Prisle, N. L., Kulmala, M., Riipinen, I., Bilde, M., Kerminen, V.-M., and Petäjä, T.:
8 Hygroscopicity, CCN and volatility properties of submicron atmospheric aerosol in a boreal
9 forest environment during the summer of 2010, *Atmos. Chem. Phys.*, 14, 4733-4748,
10 <https://doi.org/10.5194/acp-14-4733-2014>, 2014.

11
12 Horvath, H., Kasahara, M., Tohno, S., Olmo, F. J., Lyamani, H., Alados-Arboledas, L.,
13 Quirantes A., and Cachorro, V.: Relationship between fraction of backscattered light and
14 asymmetry parameter, *J. Aerosol Sci.*, 91, 43–53, 2016.

15
16 Hudson, J. G.: Cloud condensation nuclei, *J. Appl. Meteorol.*, 32, 596–607, 1993.

17
18 Hudson, J. G.: Variability of the relationship between particle size and cloud-nucleating ability,
19 *Geophys. Res. Lett.*, 34, 08801, doi:10.1029/2006GL028850, 2007.

20
21 Jefferson, A.: Empirical estimates of CCN from aerosol optical properties at four remote sites,
22 *Atmos. Chem. Phys.*, 10, 6855-6861, <https://doi.org/10.5194/acp-10-6855-2010>, 2010.

23
24 Jefferson, A.: Aerosol observing system (AOS) handbook, ARMTR-014, US Dep. of Energy,
25 Washington, D. C., 2011

26
27 Kammermann, L., Gysel, M., Weingartner, E., Herich, H., Cziczo, D. J., Holst, T.,
28 Svenningsson, B., Arneth, A., and Baltensperger, U.: Sub-arctic atmospheric aerosol
29 composition 3: Measured and modeled properties of cloud condensation nuclei (CCN), *J.*
30 *Geophys. Res.*, 115, D04202, doi:10.1029/2009JD012447, 2010.

1
2
3
4
5
6
7
8
9
10
11
12
13
14
15
16
17
18
19
20
21
22
23
24
25
26
27
28
29
30

Kassianov, E., Barnard, J., Pekour, M., Berg, L. K., Shilling, J., Flynn, C., Mei, F., and Jefferson, A.: Simultaneous retrieval of effective refractive index and density from size distribution and light-scattering data: weakly absorbing aerosol, *Atmos. Meas. Tech.*, 7, 3247-3261, <https://doi.org/10.5194/amt-7-3247-2014>, 2014.

Kerminen, V.-M., Paramonov, M., Anttila, T., Riipinen, I., Fountoukis, C., Korhonen, H., Asmi, E., Laakso, L., Lihavainen, H., Swietlicki, E., Svenningsson, B., Asmi, A., Pandis, S. N., Kulmala, M., and Petäjä, T.: Cloud condensation nuclei production associated with atmospheric nucleation: a synthesis based on existing literature and new results, *Atmos. Chem. Phys.*, 12, 12037-12059, <https://doi.org/10.5194/acp-12-12037-2012>, 2012.

King, M. D., Kaufman, Y. J., Tanré, D., and Nakajima, T.: Remote sensing of tropospheric aerosols from space: Past, present, and future, *B. Am. Meteorol. Soc.*, 80, 2229–2259, 1999.

Kuang, C.: TSI Model 3936 Scanning Mobility Particle Spectrometer Instrument Handbook, United States, doi:10.2172/1245993, <https://www.osti.gov/servlets/purl/1245993>, 2016.

Kulmala, M., Laaksonen, A., Korhonen, P., Vesala, T., Ahonen, T., and Barrett, J. C.: The effect of atmospheric nitric acid vapor on cloud condensation nuclei activation, *J. Geophys. Res.*, 98, 22949–22958, 1993.

Kulmala, M., Vehkamäki, H., Petäjä, T., Dal Maso, M., Lauri, A., Kerminen, V.M., Birmili, W. and McMurry, P.H.: Formation and growth rates of ultrafine atmospheric particles: A review of observations, *J. Aerosol Sci.*, 35, 143–176, 2004

Liu, H., Pinker, R. T., Chin, M., Holben, B., and Remer, L.: Synthesis of information on aerosol optical properties, *J. Geophys. Res.*, 113, D07206, doi:10.1029/2007JD008735, 2008.

Liu, J. and Li, Z.: Estimation of cloud condensation nuclei concentration from aerosol optical

1 quantities: influential factors and uncertainties, *Atmos. Chem. Phys.*, 14, 471–483,
2 <https://doi.org/10.5194/acp-14-471-2014>, 2014.

3
4 Luoma, K., Virkkula, A., Aalto, P., Petäjä, T., and Kulmala, M.: Over a ten-year record of
5 aerosol optical properties at SMEAR II, *Atmos. Chem. Phys. Discuss.*,
6 <https://doi.org/10.5194/acp-2018-981>, in review, 2018.

7
8 Ma, N., Birmili, W., Müller, T., Tuch, T., Cheng, Y. F., Xu, W. Y., Zhao, C. S., and Wiedensohler,
9 A.: Tropospheric aerosol scattering and absorption over central Europe: a closure study for the
10 dry particle state, *Atmos. Chem. Phys.*, 14, 6241–6259, [https://doi.org/10.5194/acp-14-6241-](https://doi.org/10.5194/acp-14-6241-2014)
11 2014, 2014.

12
13 Ma, N., Zhao, C., Tao, J., Wu, Z., Kecorius, S., Wang, Z., Größ, J., Liu, H., Bian, Y., Kuang, Y.,
14 Teich, M., Spindler, G., Müller, K., van Pinxteren, D., Herrmann, H., Hu, M., and Wiedensohler,
15 A.: Variation of CCN activity during new particle formation events in the North China Plain,
16 *Atmos. Chem. Phys.*, 16, 8593–8607, <https://doi.org/10.5194/acp-16-8593-2016>, 2016.

17
18 Mather, J. H. and Voyles, J. W.: The Arm Climate Research Facility: A Review of Structure and
19 Capabilities, *Bull. Amer. Meteor. Soc.*, 94, 377–392, 2013.

20
21 Meng, J. W., Yeung, M. C., Li, Y. J., Lee, B. Y. L., and Chan, C. K.: Size-resolved cloud
22 condensation nuclei (CCN) activity and closure analysis at the HKUST Supersite in Hong Kong,
23 *Atmos. Chem. Phys.*, 14, 10267–10282, <https://doi.org/10.5194/acp-14-10267-2014>, 2014.

24
25 Mugnai, A. and Wiscombe, W.: Scattering from nonspherical Chebyshev
26 particles. I: cross sections, single-scattering albedo, asymmetry factor, and backscattered
27 fraction, *Appl. Opt.*, 25, 1235–1244, 1986

28
29 Paramonov, M., Kerminen, V.-M., Gysel, M., Aalto, P. P., Andreae, M. O., Asmi, E.,
30 Baltensperger, U., Bougiatioti, A., Brus, D., Frank, G. P., Good, N., Gunthe, S. S., Hao, L.,

1 Irwin , M , Jaatinen , A , Juranyi , Z , King , S M , Kortelainen , A , Kristensson , A , Lihavainen ,
2 H , Kulmala , M , Lohmann , U , Martin , S T , McFiggans , G , Mihalopoulos , N , Nenes , A ,
3 O'Dowd , C D , Ovadnevaite , J , Petaja , T , Poschl , U , Roberts , G C , Rose , D , Svenningsson ,
4 B , Swietlicki , E , Weingartner , E , Whitehead , J , Wiedensohler , A , Wittbom , C & Sierau ,
5 B 2015 , ' A synthesis of cloud condensation nuclei counter (CCNC) measurements within the
6 EUCAARI network ' Atmospheric Chemistry and Physics , vol. 15 , no. 21 , pp. 12211-12229 .
7 <https://doi.org/10.5194/acp-15-12211-2015>.

8

9 Petters, M. D., and S. M. Kreidenweis, S. M.: A single parameter representation of hygroscopic
10 growth and cloud condensation nucleus activity Atmos. Chem. Phys., 7, 1961–1971,
11 doi:10.5194/acp-7-1961-2007, 2007.

12

13 Pringle, K. J., Tost, H., Pozzer, A., Pöschl, U., and Lelieveld, J.: Global distribution of the
14 effective aerosol hygroscopicity parameter for CCN activation, Atmos. Chem. Phys., 10, 5241-
15 5255, <https://doi.org/10.5194/acp-10-5241-2010>, 2010.

16

17 Pöhlker, M. L., Pöhlker, C., Ditas, F., Klimach, T., Hrabec de Angelis, I., Araújo, A., Brito, J.,
18 Carbone, S., Cheng, Y., Chi, X., Ditz, R., Gunthe, S. S., Kesselmeier, J., Könemann, T., Lavrič,
19 J. V., Martin, S. T., Mikhailov, E., Moran-Zuloaga, D., Rose, D., Saturno, J., Su, H., Thalman,
20 R., Walter, D., Wang, J., Wolff, S., Barbosa, H. M. J., Artaxo, P., Andreae, M. O., and Pöschl,
21 U.: Long-term observations of cloud condensation nuclei in the Amazon rain forest – Part 1:
22 Aerosol size distribution, hygroscopicity, and new model parametrizations for CCN prediction,
23 Atmos. Chem. Phys., 16, 15709-15740, <https://doi.org/10.5194/acp-16-15709-2016>, 2016.

24

25 Qi, X. M., Ding, A. J., Nie, W., Petäjä, T., Kerminen, V.-M., Herrmann, E., Xie, Y. N., Zheng,
26 L. F., Manninen, H., Aalto, P., Sun, J. N., Xu, Z. N., Chi, X. G., Huang, X., Boy, M., Virkkula,
27 A., Yang, X.-Q., Fu, C. B., and Kulmala, M.: Aerosol size distribution and new particle
28 formation in the western Yangtze River Delta of China: 2 years of measurements at the
29 SORPES station, Atmos. Chem. Phys., 15, 12445-12464, [https://doi.org/10.5194/acp-15-](https://doi.org/10.5194/acp-15-12445-2015)
30 12445-2015, 2015.

1

2 Rose, D., Gunthe, S. S., Mikhailov, E., Frank, G. P., Dusek, U., Andreae, M. O., and Pöschl, U.:
3 Calibration and measurement uncertainties of a continuous-flow cloud condensation nuclei
4 counter (DMT-CCNC): CCN activation of ammonium sulfate and sodium chloride aerosol
5 particles in theory and experiment, *Atmos. Chem. Phys.*, 8, 1153-1179,
6 <https://doi.org/10.5194/acp-8-1153-2008>, 2008.

7

8 Schmale, J., Henning, S., Henzing, B., Keskinen, H., Sellegri, K., Ovadnevaite, J., Bougiatioti,
9 A., Kalivitis, N., Stavroulas, I., Jefferson, A., Park, M., Schlag, P., Kristensson,
10 A., Iwamoto, Y., Pringle, K., Reddington, C., Aalto, P., Äijälä, M.,
11 Baltensperger, U., Bialek, J., Birmili, W., Bukowiecki, N., Ehn, M., Fjæraa, A. M., Fiebig,
12 M., Frank, G., Fröhlich, R., Frumau, A., Furuya, M., Hammer, E., Heikkinen, L., Herrmann, E.,
13 Holzinger, R., Hyono, H., Kanakidou, M., Kiendler-Scharr, A., Kinouchi, K., Kos, G., Kulmala,
14 M., Mihalopoulos, N., Motos, G., Nenes, A., O'Dowd, C., Paramonov, M., Petäjä, T., Picard,
15 D., Poulain, L., Prévôt, A. S. H., Slowik, J., Sonntag, A., Swietlicki, E., Svenningsson, B.,
16 Tsurumaru, H., Wiedensohler, A., Wittbom, C., Ogren, J. A., Matsuki, A., Yum, S. S., Myhre,
17 C. L., Carslaw, K., Stratmann, F. and Gysel, M.: Collocated observations of cloud
18 condensation nuclei, particle size distributions, and chemical composition, *Sci.*
19 *Data*, 4, 170003, doi:10.1038/sdata.2017.3, 2017a.

20

21 Schmale, J., Henning, S., Decesari, S., Henzing, B., Keskinen, H., Sellegri, K., Ovadnevaite, J.,
22 Pöhlker, M. L., Brito, J., Bougiatioti, A., Kristensson, A., Kalivitis, N., Stavroulas, I., Carbone,
23 S., Jefferson, A., Park, M., Schlag, P., Iwamoto, Y., Aalto, P., Äijälä, M., Bukowiecki, N., Ehn,
24 M., Frank, G., Fröhlich, R., Frumau, A., Herrmann, E., Herrmann, H., Holzinger, R., Kos, G.,
25 Kulmala, M., Mihalopoulos, N., Nenes, A., O'Dowd, C., Petäjä, T., Picard, D., Pöhlker, C.,
26 Pöschl, U., Poulain, L., Prévôt, A. S. H., Swietlicki, E., Andreae, M. O., Artaxo, P.,
27 Wiedensohler, A., Ogren, J., Matsuki, A., Yum, S. S., Stratmann, F., Baltensperger, U., and
28 Gysel, M.: Long-term cloud condensation nuclei number concentration, particle number size
29 distribution and chemical composition measurements at regionally representative observatories,
30 *Atmos. Chem. Phys.*, 18, 2853-2881, <https://doi.org/10.5194/acp-18-2853-2018>, 2018.

1
2
3
4
5
6
7
8
9
10
11
12
13
14
15
16
17
18
19
20
21
22
23
24
25
26
27
28
29
30

Schuster, G. L., Dubovik, O., and Holben, B. N.: Angstrom exponent and bimodal aerosol size distributions, *J. Geophys. Res.*, 111, D07207, doi:10.1029/2005JD006328, 2006.

Schwartz, S. E., Charlson, R. J., Kahn, R. A., Ogren, J. A., and Rodhe, H.: Why hasn't Earth warmed as much as expected?, *J. Climate*, 23, 2453–2464, 2010.

Shen, Y., Virkkula, A., Ding, A., Wang, J., Chi, X., Nie, W., Qi, X., Huang, X., Liu, Q., Zheng, L., Xu, Z., Petäjä, T., Aalto, P. P., Fu, C., and Kulmala, M.: Aerosol optical properties at SORPES in Nanjing, east China, *Atmos. Chem. Phys.*, 18, 5265-5292, <https://doi.org/10.5194/acp-18-5265-2018>, 2018.

Shinozuka, Y., Clarke, A. D., DeCarlo, P. F., Jimenez, J. L., Dunlea, E. J., Roberts, G. C., Tomlinson, J. M., Collins, D. R., Howell, S. G., Kapustin, V. N., McNaughton, C. S., and Zhou, J.: Aerosol optical properties relevant to regional remote sensing of CCN activity and links to their organic mass fraction: airborne observations over Central Mexico and the US West Coast during MILAGRO/INTEX-B, *Atmos. Chem. Phys.*, 9, 6727-6742, <https://doi.org/10.5194/acp-9-6727-2009>, 2009.

Shinozuka, Y., Clarke, A. D., Nenes, A., Jefferson, A., Wood, R., McNaughton, C. S., Ström, J., Tunved, P., Redemann, J., Thornhill, K. L., Moore, R. H., Latham, T. L., Lin, J. J., and Yoon, Y. J.: The relationship between cloud condensation nuclei (CCN) concentration and light extinction of dried particles: indications of underlying aerosol processes and implications for satellitebased CCN estimates, *Atmos. Chem. Phys.*, 15, 7585–7604, <https://doi.org/10.5194/acp-15-7585-2015>, 2015

Sihto, S.-L., Kulmala, M., Kerminen, V.-M., Dal Maso, M., Petäjä, T., Riipinen, I., Korhonen, H., Arnold, F., Janson, R., Boy, M., Laaksonen, A., and Lehtinen, K. E. J.: Atmospheric sulphuric acid and aerosol formation: implications from atmospheric measurements for nucleation and early growth mechanisms, *Atmos. Chem. Phys.*, 6, 4079-4091,

1 <https://doi.org/10.5194/acp-6-4079-2006>, 2006.

2

3 Sihto, S.-L., Mikkilä, J., Vanhanen, J., Ehn, M., Liao, L., Lehtipalo, K., Aalto, P. P., Duplissy,
4 J., Petaja, T., Kerminen, V.-M., Boy, M., and Kulmala, M.: Seasonal variation of CCN
5 concentrations and aerosol activation properties in boreal forest, *Atmos. Chem. Phys.*, 11,
6 13269–13285, doi:10.5194/acp-11-13269-2011, 2011.

7

8 Tao, J., Zhao, C., Kuang, Y., Zhao, G., Shen, C., Yu, Y., Bian, Y., and Xu, W.: A new method
9 for calculating number concentrations of cloud condensation nuclei based on measurements of
10 a three-wavelength humidified nephelometer system, *Atmos. Meas. Tech.*, 11, 895-906,
11 <https://doi.org/10.5194/amt-11-895-2018>, 2018.

12

13 Twomey, S.: The influence of cloud nucleus population on the microstructure and stability of
14 convective clouds, *Tellus*, 11, 408–411, 1959.

15

16 Uin, J.: Integrating Nephelometer Instrument Handbook, United States. doi:10.2172/1246075.
17 <https://www.osti.gov/servlets/purl/1246075>, 2016a

18

19 Uin, J.: Cloud Condensation Nuclei Particle Counter (CCN) Instrument Handbook, United
20 States. doi:10.2172/1251411. <https://www.osti.gov/servlets/purl/1251411>, 2016b

21

22 Virkkula, A., Backman, J., Aalto, P. P., Hulkkonen, M., Riuttanen, L., Nieminen, T., dal Maso,
23 M., Sogacheva, L., de Leeuw, G., and Kulmala, M.: Seasonal cycle, size dependencies, and
24 source analyses of aerosol optical properties at the SMEAR II measurement station in Hyytiälä,
25 Finland, *Atmos. Chem. Phys.*, 11, 4445-4468, <https://doi.org/10.5194/acp-11-4445-2011>, 2011.

26

27 Wang, J., Cubison, M. J., Aiken, A. C., Jimenez, J. L., and Collins, D. R.: The importance of
28 aerosol mixing state and size-resolved composition on CCN concentration and the variation of
29 the importance with atmospheric aging of aerosols, *Atmos. Chem. Phys.*, 10, 7267–7283,
30 doi:10.5194/acp-10-7267-2010, 2010.

1

2 Wiscombe, W. J., and Grams, G. W.: The backscattered fraction in two-stream approximations,

3 J. Atmos. Sci., 33, 2440– 2451, 1976.

4

5

1 **Tables**

2

3 **Table 1. Site and data description**

Dataset	Description	Location	Period	CCN		Size distribution		AOPs	
				Instrument	SS	Instrument	size range	Instrument	inlet
SMEAR II	Boreal Forest, Finland	61°51' N, 24°17' E, 179m	2016.1.1-2016.12.31	CCN-100	0.1%, 0.2%, 0.5% and 1.0%	DMPS custom-made	3-1000nm	Nephelometer TSI-3563	PM1, PM10
SORPES	Urban agglomerations, China	32°07' N, 118°56'E, 40m	2016.06.01-2017.05.31	CCN-200	0.1%, 0.2%, 0.4%, and 0.8%	DMPS custom-made	6-800nm	Nephelometer Aurora-3000	TSP
PGH ^a	Ganges Valley, India	29°22' N, 79°27' E, 1936m	2011.11.01-2013.03.25	CCN-100	0.12%, 0.22%, 0.48% and 0.78%	NA	NA	Nephelometer TSI-3563	PM1, PM10
PVC ^b	Cape Cod, USA	42°2' N, 70°3' W, 43m	2012.07.16-2012.09.30	CCN-100	0.15%, 0.25%, 0.4% and 1.0%	SMPS TSI-3936	11-465nm*	Nephelometer TSI-3563	PM1, PM10
MAO ^c	Downwind Manaus City, Brazil	3°13' S, 60°36' W, 50m	2014.01.29-2014.12.31	CCN-100	0.25%, 0.4%, 0.6% and 1.1%	SMPS TSI-3936	11-465nm*	Nephelometer TSI-3563	PM1, PM10
ASI ^d	Ascension Island, Atlantic Ocean	7°58' S, 14°21' W, 341m	2016.06.01-2017.10.19	CCN-100	0.1%, 0.2%, 0.4%, and 0.8%	SMPS TSI-3936	11-465nm*	Nephelometer TSI-3563	PM1, PM10

^a use products: aipavglogrenM1.c1., and aosccnavgM1.c2.

^b use products: aipavglogrenM1.s1., noaaaosccn100M1.b1., and aossmpls1.a1.

^c use products: aiplogrenM1.c1., aosccn1colM1.b1., and aossmpls1.a1.

^d use products: aosnephdryM1.b1., aosccn2colaavgM1.b1., and aossmplsM1.a1.

4 * vary slightly

5

6 **Table 2. Descriptive statistics of AOPs of PM10 aerosol and N_{CCN} at the different sites. σ_{sp} :**
7 **total scattering coefficient of green light ($\lambda = 550$ nm or 525 nm), in Mm^{-1} ; BSF: backscatter**
8 **fraction of green light; SAE: scattering Ångström exponent between blue and red light. The**
9 **N_{CCN} statistics in $\# cm^{-3}$ are presented for four supersaturations (SS) at each site. The numbers**
10 **are the averages and standard deviations.**

	σ_{sp}	AOPs		CCN				
		BSF	SAE	#1	#2	#3	#4	
SMEAR II	14±14	0.15±0.03	2.11±0.67	SS:	0.10%	0.20%	0.50%	1.00%
				N_{CCN} :	129±99	303±229	514±388	740±511
SORPES	270±188	0.11±0.02	1.45±0.33	SS:	0.10%	0.20%	0.40%	0.80%
				N_{CCN} :	974±632	2377±1244	4199±1915	5363±2245
PGH	239±215	0.07±0.01	0.53±0.30	SS:	0.12%	0.22%	0.48%	0.78%
				N_{CCN} :	325±296	935±621	2359±1391	2882±1707
PVC	27±22	0.13±0.03	1.79±0.52	SS:	0.15%	0.25%	0.40%	1.00%
				N_{CCN} :	515±361	864±603	1163±774	1766±1020
MAO	24±19	0.14±0.02	1.00±0.55	SS:	0.25%	0.40%	0.60%	1.10%
				N_{CCN} :	448±377	783±693	1034±923	1251±1068
ASI	20±13	0.14±0.01	0.73±0.41	SS:	0.10%	0.20%	0.40%	0.80%
				N_{CCN} :	113±79	234±175	271±199	319±203

11

12

13

14

15

1 Table 3. The slopes and offsets of ordinary linear regressions of $R_{CCN/\sigma}$ vs. BSF at the different
 2 supersaturation SS at the studied sites. s.e.: standard error of the respective coefficient obtained
 3 from the linear regressions. The unit of the coefficients is $[N_{CCN}]/[\sigma_{sp}] = \text{cm}^{-3}/\text{Mm}^{-1}$.

$R_{CCN/s} = aBSF + b$			
	SS (%)	a \pm s.e.	b \pm s.e.
SMEAR II	0.10	91 \pm 3	-2.9 \pm 0.4
	0.20	433 \pm 5	-38.6 \pm 0.7
	0.50	867 \pm 10	-86.4 \pm 1.5
	1.00	1155 \pm 17	-115.8 \pm 2.5
SORPES	0.10	62 \pm 2	-2.6 \pm 0.2
	0.20	266 \pm 4	-18.4 \pm 0.4
	0.40	531 \pm 7	-39.1 \pm 0.8
	0.80	738 \pm 11	-55.9 \pm 1.2
PGH	0.12	-18 \pm 1	2.6 \pm 0.1
	0.22	24 \pm 3	2.8 \pm 0.2
	0.48	244 \pm 12	-4.4 \pm 0.8
	0.78	344 \pm 14	-8.3 \pm 1.0
PVC	0.15	417 \pm 9	-30.2 \pm 1.1
	0.25	793 \pm 17	-61.7 \pm 2.1
	0.40	1176 \pm 25	-95.3 \pm 3.1
	1.00	1945 \pm 43	-161.4 \pm 5.3
MAO	0.25	273 \pm 5	-19.0 \pm 0.7
	0.40	544 \pm 8	-42.9 \pm 1.2
	0.60	678 \pm 13	-50.9 \pm 1.8
	1.10	868 \pm 32	-58.3 \pm 4.3
ASI	0.10	22 \pm 2	2.2 \pm 0.2
	0.20	105 \pm 3	-3.6 \pm 0.5
	0.40	127 \pm 4	-5.0 \pm 0.6
	0.80	136 \pm 4	-4.0 \pm 0.6

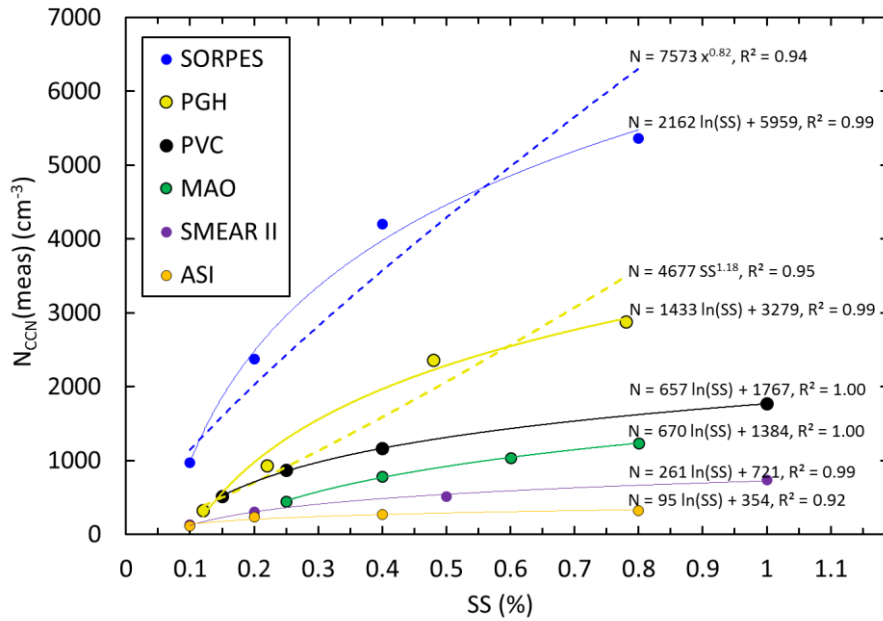
4
5

6 Table 4. The coefficients a_0 , a_1 , b_0 and b_1 obtained from the fitting of $a = a_1 \ln(SS) + a_0$ and $b =$
 7 $b_1 \ln(SS) + b_0$ with the data in Table 3. The unit of the coefficients is $[N_{CCN}]/[\sigma_{sp}] = \text{cm}^{-3}/\text{Mm}^{-1}$.
 8 s.e.: standard error of the respective coefficient obtained from the regressions. SAE: scattering
 9 Ångström exponent of PM10 aerosol.

SITE	$R_{CCN/\sigma} = (a_1 \ln(SS) + a_0)BSF + b_1 \ln(SS) + b_0$				SAE	
	$a_1 \pm$ s.e.	$a_0 \pm$ s.e.	$b_1 \pm$ s.e.	$b_0 \pm$ s.e.	average \pm std	median
SMEAR II	464 \pm 11	1170 \pm 16	-49 \pm 1.5	-118 \pm 2.1	2.11 \pm 0.67	2.22
SORPES	331 \pm 12	817 \pm 18	-26 \pm 0.9	-62 \pm 1.4	1.45 \pm 0.33	1.50
PGH	205 \pm 30	385 \pm 41	-6.3 \pm 1.5	-9.1 \pm 2.0	0.53 \pm 0.30	0.57
PVC	810 \pm 17	1933 \pm 21	-70 \pm 1.7	-160 \pm 2.1	1.79 \pm 0.52	1.91
MAO	393 \pm 45	858 \pm 40	-25 \pm 6.6	-60 \pm 5.8	1.00 \pm 0.55	1.09
ASI	52 \pm 17	164 \pm 26	-2.9 \pm 1.6	-6.3 \pm 2.3	0.73 \pm 0.41	0.64

10
11
12
13
14

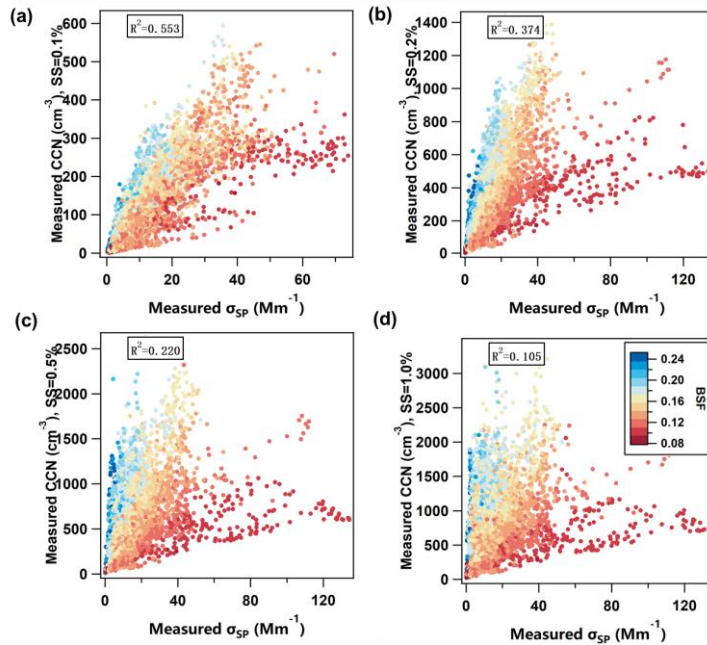
1 **FIGURES**



2

3 **Figure 1. Averages of the measured N_{CCN} at the six sites at the station-specific supersaturations**

4 **of the CCN counters and a logarithmic fitting to the data.**



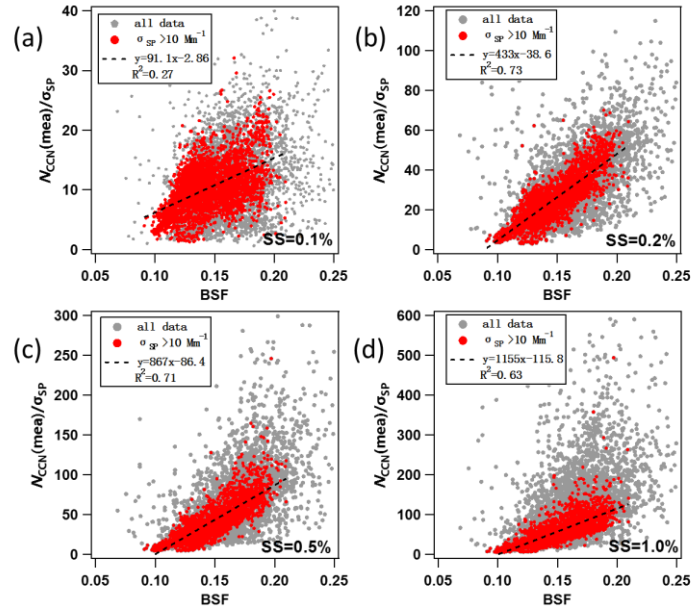
5

6 **Figure 2. Measured CCN number concentration $N_{CCN}(\text{meas})$ vs. PM_{10} scattering coefficient σ_{SP}**

7 **at $\lambda = 550$ nm at SMEAR II at four supersaturations (SS): a) 0.1 %, b) 0.2 %, c) 0.5 % and d) 1.0 %.**

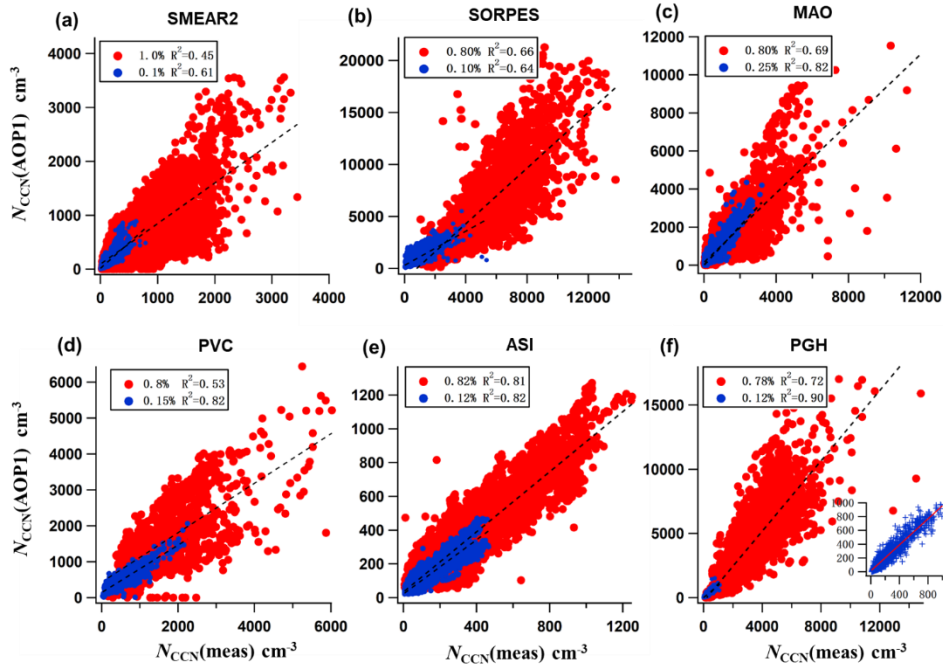
8 **Colorcoding: backscatter fraction (BSF) at $\lambda = 550$ nm.**

9



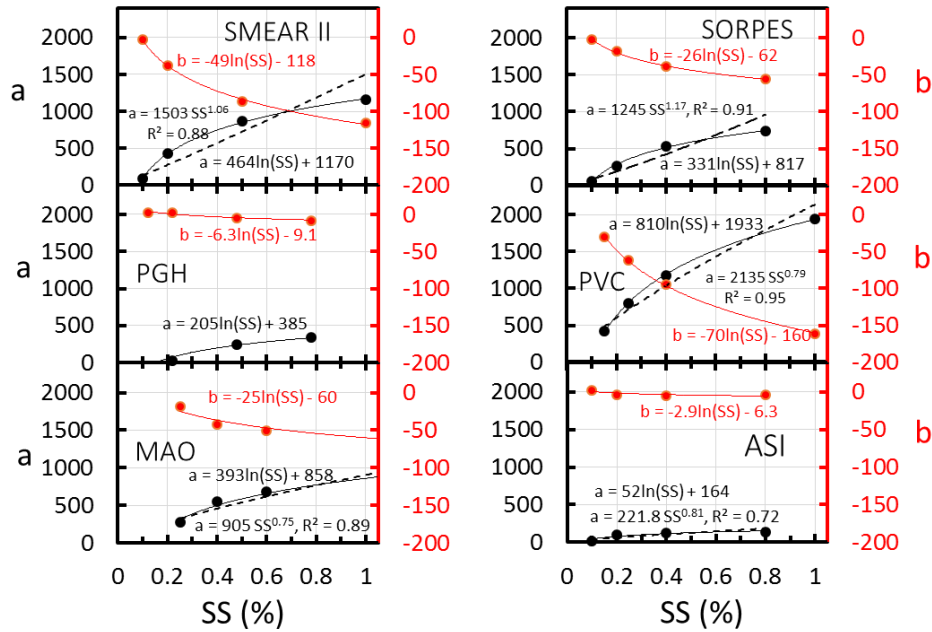
1

2 Figure 3. Relationship between $R_{CCN/\sigma}$ ($= N_{CCN}(\text{meas})/\alpha_{sp}$) and BSF at SMEAR II at four
 3 supersaturations (SS): a) 0.1 %, b) 0.2 %, c) 0.5 % and d) 1.0 %. Grey symbols: all data, red
 4 symbols: data at $\sigma_{sp} > 10 \text{ Mm}^{-1}$. Both σ_{sp} and BSF were measured at $\lambda = 550 \text{ nm}$.



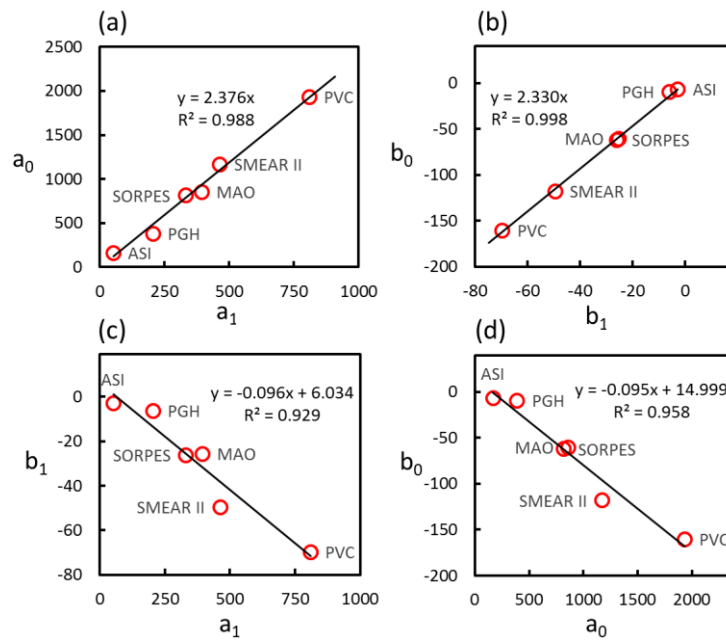
5

6 Figure 4. $N_{CCN}(\text{AOP}_1)$ vs. $N_{CCN}(\text{meas})$ at a) SMEAR II, b) SORPES, c) MAO, d) PVC, e) ASI and f)
 7 PGH. $N_{CCN}(\text{AOP})$ was calculated by using the slopes and offsets a and b of the linear regressions
 8 $R_{CCN/\sigma} = a\text{BSF} + b$ in Table 3 for two supersaturations (blue symbols: low SS, red symbols: high
 9 SS).



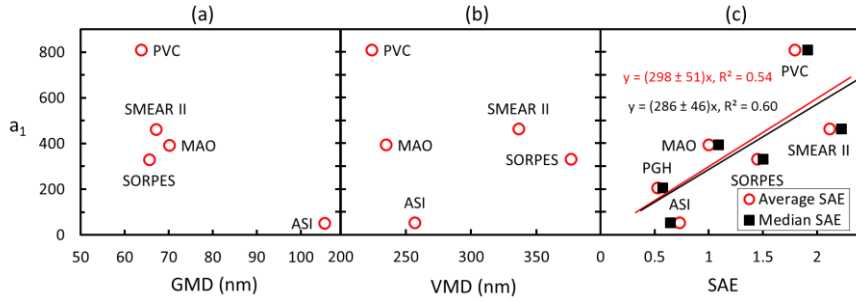
1
2
3
4
5
6
7

Figure 5. The the slopes and offsets a and b of the linear regressions $R_{CCN/\sigma} = aBSF + b$ of each station (Table 3) as a function of supersaturation SS . Two types of functions, a logarithmic and a power function were fitted to the coefficient a , to coefficient b only a logarithmic function. The squared correlation coefficients R^2 are shown only for the power function fittings, for the logarithmic fittings they were all > 0.99 .

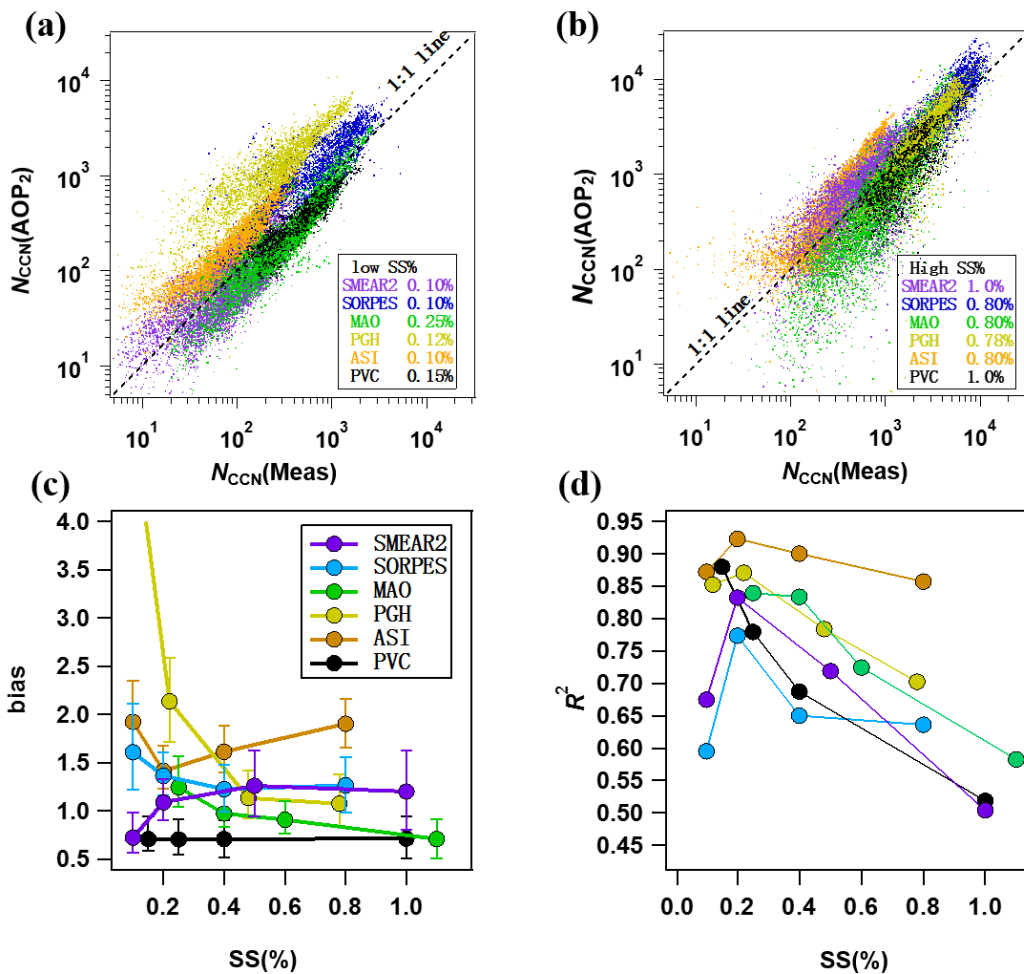


8

9 Figure 6. Relationship between the coefficients a_0 , a_1 , b_0 and b_1 of Equation (7) for each station
10 presented in Table 4 for the 6 stations. a) a_0 vs. a_1 , b) b_0 vs. b_1 , c) b_1 vs. a_1 , d) b_0 vs. a_0 .

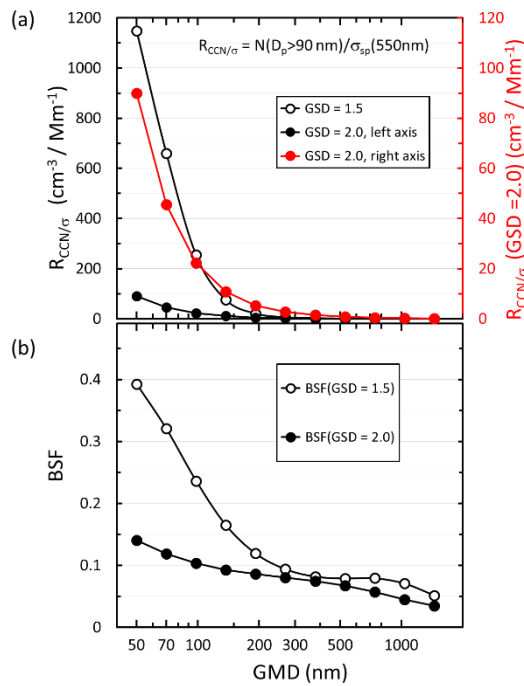


1
 2 Figure 7. Relationship of the a_1 coefficient in Equation (8) with the average a) geometric mean
 3 diameter of the PNSD data size ranges of the sites, b) volume mean diameter of the same size
 4 range, and c) PM_{10} scattering Ångström exponent (SAE).



5
 6 Figure 8. Statistics of $N_{CCN}(AOP_2)$ from parameterization in Eq. (10). $N_{CCN}(AOP_2)$ vs. $N_{CCN}(meas)$
 7 at different sites at relatively (a) low and (b) high supersaturations, (c) bias = $N_{CCN}(AOP_2) / N_{CCN}$
 8 (meas) at different sites and supersaturations, and (d) R^2 of the linear regression of $N_{CCN}(AOP_2)$
 9 vs. $N_{CCN}(meas)$ at different sites and supersaturations.

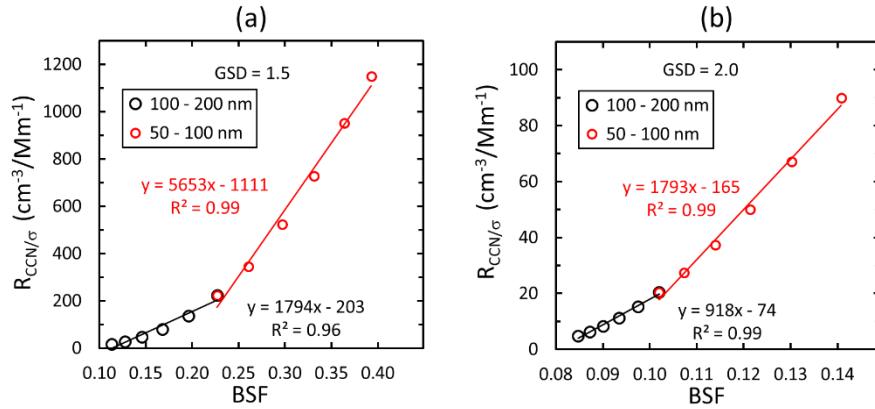
1



2

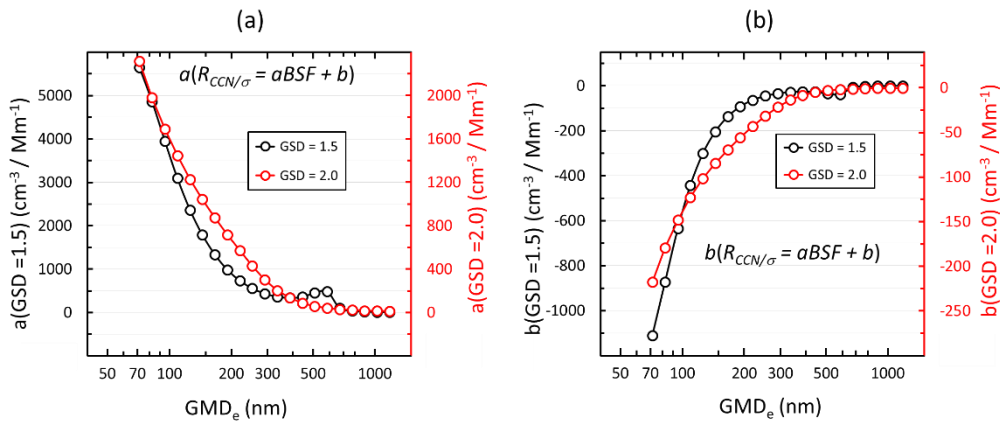
3 Figure 9. Size distribution of a) $R_{CCN/\sigma}$ and b) backscatter fraction BSF ($\lambda = 550 \text{ nm}$) of simulated
4 narrow (GSD = 1.5) and wide (GSD = 2.0) unimodal size distributions. GMD: geometric mean
5 diameter, GSD: geometric standard deviation. Note: in a) the $R_{CCN/\sigma}$ of the wide size
6 distributions are plotted twice: the black symbols and line use the left axis to emphasize the
7 big difference in the magnitudes of the wide and narrow size distributions; the red symbols
8 and line use the right axis to show that the shape of the $R_{CCN/\sigma}$ size distribution is very similar
9 to the one calculated for the narrow size distributions. $R_{CCN/\sigma}$ was calculated assuming
10 particles larger than 90 nm get activated.

11



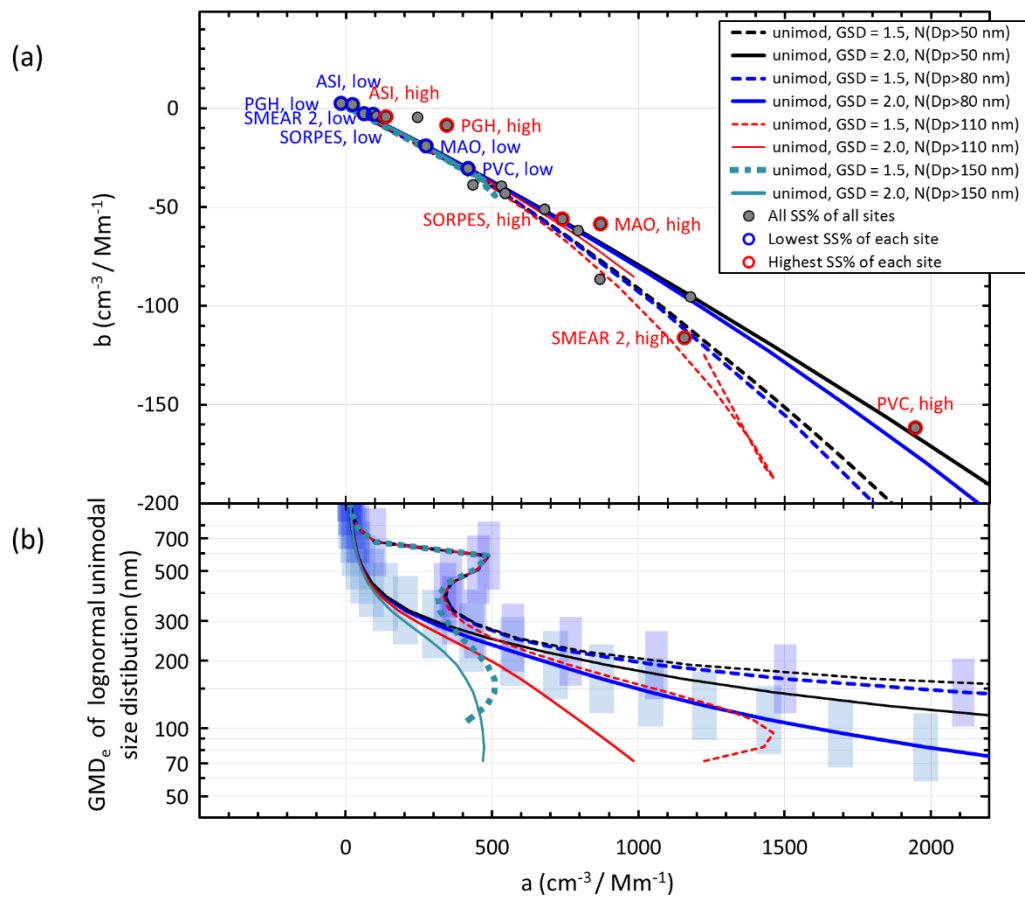
1
2
3
4
5
6
7

Figure 10. Linear regressions of $R_{CCN/\sigma}$ vs backscatter fraction BSF ($\lambda = 550$ nm) of simulated unimodal a) narrow (GSD = 1.5) and b) wide (GSD = 2.0) size distributions. The regressions were calculated assuming that the data consist of size distributions with GMD ranging from 50 to 100 nm and 100 to 200 nm. $R_{CCN/\sigma}$ was calculated assuming particles larger than 90 nm get activated.



8
9
10
11
12
13
14
15
16

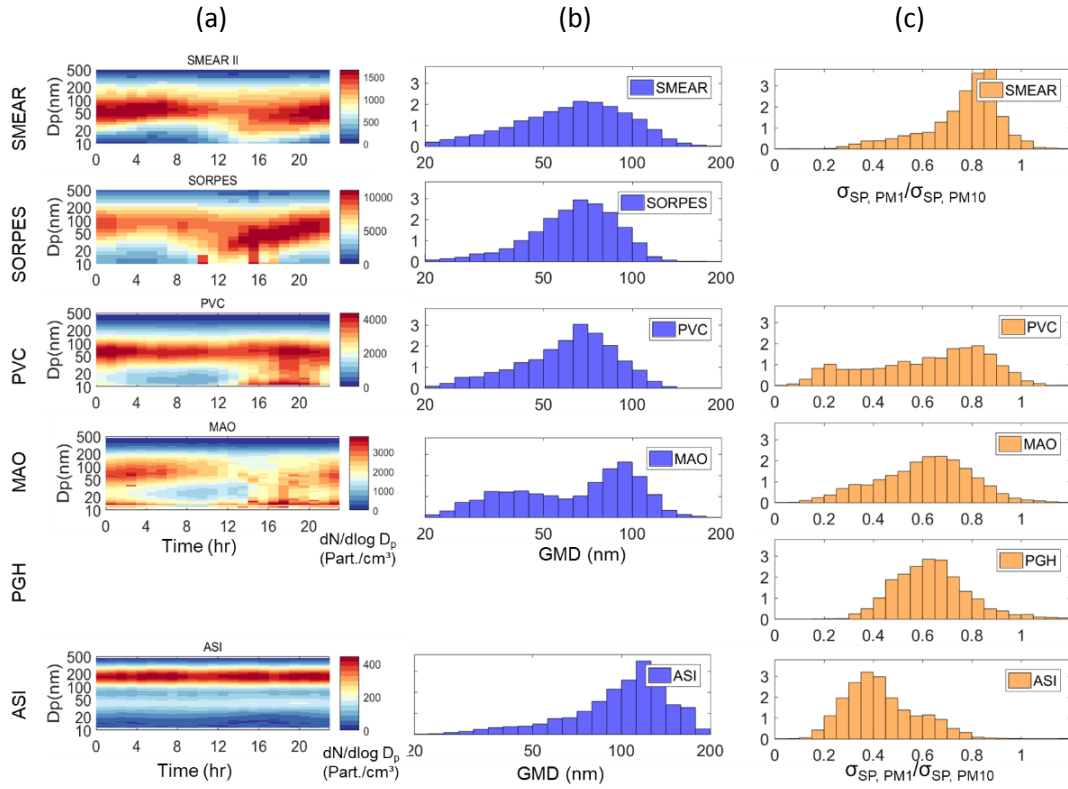
Figure 11. Size distributions of the coefficients of the linear regressions of $R_{CCN/\sigma}$ ($\lambda = 550$ nm) vs backscatter fraction BSF ($\lambda = 550$ nm) of narrow and wide size distributions. a) slopes of $R_{CCN/\sigma}$ vs. BSF, b) offsets of $R_{CCN/\sigma}$ vs. BSF. $R_{CCN/\sigma}$ was calculated assuming particles larger than 90 nm get activated. The regressions were calculated for 5 consecutive size distributions. GMD_e is the geometric mean of the range of the unimodal size distributions used for the regressions.



1
 2 Figure 12. a) Relationships of the slopes and offsets of the linear regressions of $R_{\text{CCN}/\sigma} = a\text{BSF} +$
 3 b vs. BSF of the simulated unimodal narrow (GSD = 1.5) and wide (GSD = 2.0) size distributions
 4 and those obtained from the similar regressions of the station data (Table 3). b) Equivalent
 5 geometric mean diameter (GMD_e) of the unimodal modes used for the linear regression vs.
 6 the slope of the linear regression of $R_{\text{CCN}/\sigma}$ vs. BSF. The vertical error bars show the ranges of
 7 the GMD_e s of the unimodal size distributions used in the respective linear regressions. $R_{\text{CCN}/\sigma}$
 8 was calculated for the activation diameters of 50 nm, 80 nm, 110nm, and 150 nm.

9
 10

1



2

3 Figure 13. Analyses of particle size distributions at the six sites. a) Average diurnal cycle of
4 PNSD and b) normalized size distribution of GMD at SMEAR II, SORPES, PVC, and ASI, c)
5 normalized frequency distribution of $\sigma_{sp}(PM_1)/\sigma_{sp}(PM_{10})$ at SMEAR II, PVC, MAO, PGH and ASI.
6